Neuron

Article

Nucleocytoplasmic mRNA redistribution accompanies RNA binding protein mislocalization in ALS motor neurons and is restored by VCP ATPase inhibition

Graphical abstract

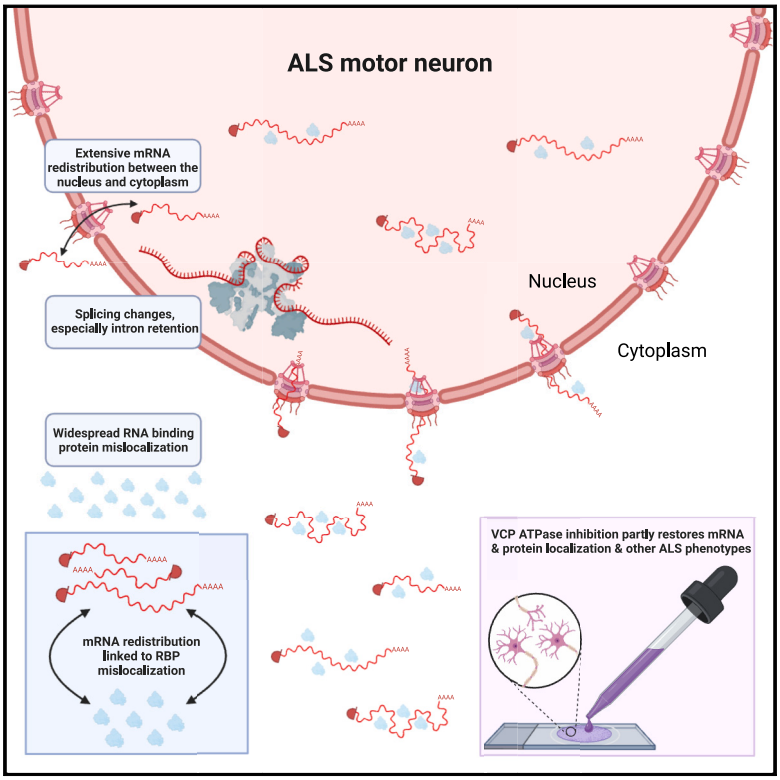

Highlights

- ALS motor neurons show extensive nucleocytoplasmic alterations in mRNA and protein
- RBP mislocalization is linked to mRNA redistribution in ALS neurons
- VCP inhibition partly restored mRNA and protein localization and other ALS phenotypes

Authors

Oliver J. Ziff, Jasmine Harley, Yiran Wang, ..., Anob M. Chakrabarti, Gavin Kelly, Rickie Patani

Correspondence

o.ziff@ucl.ac.uk (O.J.Z.), rickie.patani@ucl.ac.uk (R.P.)

In brief

Ziff et al. uncover widespread mRNA redistribution and mislocalization of RNA-binding proteins in ALS motor neurons. Their study highlights the potential of VCP ATPase inhibition in partially restoring mRNA and protein distribution, providing insights into ALS pathogenesis and a promising therapeutic target.

Ziff et al., 2023, Neuron *111*, 1–17
October 4, 2023 © 2023 The Author(s). Published by Elsevier Inc.
https://doi.org/10.1016/j.neuron.2023.06.019

CellPress

Please cite this article in press as: Ziff et al., Nucleocytoplasmic mRNA redistribution accompanies RNA binding protein mislocalization in ALS motor neurons and is restored by VCP ATPase inhibition, Neuron (2023), https://doi.org/10.1016/j.neuron.2023.06.019

Neuron

CellPress
OPEN ACCESS

Article

Nucleocytoplasmic mRNA redistribution accompanies RNA binding protein mislocalization in ALS motor neurons and is restored by VCP ATPase inhibition

Oliver J. Ziff,[1,2,3,5,*] Jasmine Harley,[1,2,4,5] Yiran Wang,[1,2,5] Jacob Neeves,[1,2,5] Giulia Tyzack,[1,2] Fairouz Ibrahim,[1] Mark Skehel,[1] Anob M. Chakrabarti,[1] Gavin Kelly,[1,2] and Rickie Patani[1,2,3,6,*]
[1]The Francis Crick Institute, 1 Midland Road, NW1 1AT London, UK
[2]Department of Neuromuscular Diseases, Queen Square Institute of Neurology, University College London, WC1N 3BG London, UK
[3]National Hospital for Neurology and Neurosurgery, University College London NHS Foundation Trust, WC1N 3BG London, UK
[4]Institute of Molecular and Cell Biology, A*STAR Research Entities, Singapore 138673, Singapore
[5]These authors contributed equally
[6]Lead contact
*Correspondence: o.ziff@ucl.ac.uk (O.J.Z.), rickie.patani@ucl.ac.uk (R.P.)
https://doi.org/10.1016/j.neuron.2023.06.019

SUMMARY

Amyotrophic lateral sclerosis (ALS) is characterized by nucleocytoplasmic mislocalization of the RNA-binding protein (RBP) TDP-43. However, emerging evidence suggests more widespread mRNA and protein mislocalization. Here, we employed nucleocytoplasmic fractionation, RNA sequencing, and mass spectrometry to investigate the localization of mRNA and protein in induced pluripotent stem cell-derived motor neurons (iPSMNs) from ALS patients with *TARDBP* and *VCP* mutations. ALS mutant iPSMNs exhibited extensive nucleocytoplasmic mRNA redistribution, RBP mislocalization, and splicing alterations. Mislocalized proteins exhibited a greater affinity for redistributed transcripts, suggesting a link between RBP mislocalization and mRNA redistribution. Notably, treatment with ML240, a VCP ATPase inhibitor, partially restored mRNA and protein localization in ALS mutant iPSMNs. ML240 induced changes in the VCP interactome and lysosomal localization and reduced oxidative stress and DNA damage. These findings emphasize the link between RBP mislocalization and mRNA redistribution in ALS motor neurons and highlight the therapeutic potential of VCP inhibition.

INTRODUCTION

Amyotrophic lateral sclerosis (ALS) is a fatal neurodegenerative disease characterized by motor neuron degeneration and lacks effective treatments.[1] Understanding ALS pathogenesis is critical for identifying therapeutic targets.[2] The hallmark of ALS pathology is the mislocalization of TDP-43; however, other RNA-binding proteins (RBPs) such as FUS, SFPQ, heterogeneous ribonucleoprotein particles (hnRNPs), and ELAVL3 have been found to be mislocalized.[3–9] RBP mislocalization affects nucleocytoplasmic transport in ALS by interfering with nuclear pore complex (NPC) components.[10–15] Although the impact of RBP mislocalization and nucleocytoplasmic transport defects on mRNA localization is recognized, few systematic attempts to evaluate the transcriptome- and proteome-wide subcellular distribution in ALS have been conducted.[16–19]

mRNA distribution between the nucleus and cytoplasm is regulated by transcript synthesis, degradation, RNA processing, nucleocytoplasmic transport, and RBP interactions.[20–22] RBP interactions coordinate 5′ capping, intron splicing, 3′ end cleavage, and polyadenylation, facilitating nuclear export and mRNA translation.[23,24] Intron splicing in humans is coupled with nuclear export through the TREX export complex and mRNA adapters.[25,26] Thus, transcripts retaining introns are primarily detained in the nucleus, ensuring that fully processed mRNAs encounter the cytoplasmic translation machinery.[27]

The ability to differentiate patient-derived induced pluripotent stem cells (iPSCs) into motor neurons (iPSMNs) has transformed ALS modeling, enabling the study of motor-neuron-specific changes attributable to genetic backgrounds.[4,28–32] While studying whole-cell extracts has revealed gene expression changes in ALS iPSMNs, subcellular fractionation of iPSMNs into nuclear and cytoplasmic fractions allows investigation of nucleocytoplasmic distribution.[4,28–32] In this study, we assessed mRNA and protein localization in iPSMNs from healthy individuals and ALS patients with mutations in TAR DNA binding protein (*TARDBP*) or Valosin-containing pProtein (*VCP*, also known as p97). Our findings shed light on the pathobiology of ALS and uncover a potential therapeutic target.

This is an open access article under the CC BY license (http://creativecommons.org/licenses/by/4.0/).

Please cite this article in press as: Ziff et al., Nucleocytoplasmic mRNA redistribution accompanies RNA binding protein mislocalization in ALS motor neurons and is restored by VCP ATPase inhibition, Neuron (2023), https://doi.org/10.1016/j.neuron.2023.06.019

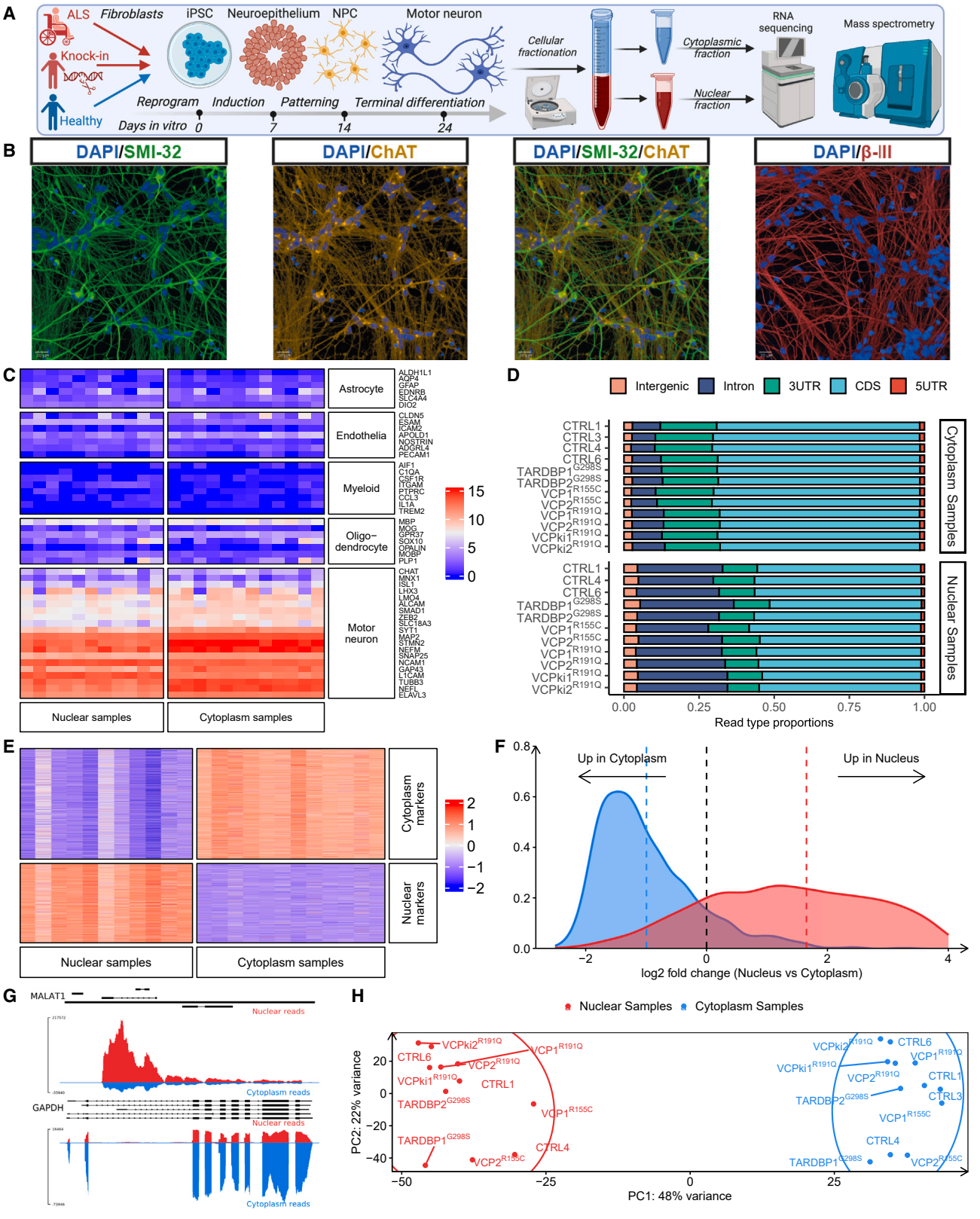

(legend on next page)

Please cite this article in press as: Ziff et al., Nucleocytoplasmic mRNA redistribution accompanies RNA binding protein mislocalization in ALS motor neurons and is restored by VCP ATPase inhibition, Neuron (2023), https://doi.org/10.1016/j.neuron.2023.06.019

CellPress
OPEN ACCESS

RESULTS

Characterization of nuclear and cytoplasmic fractions from iPSMNs

The nucleocytoplasmic localization of transcripts remains an important but unresolved issue in ALS. To address this, we examined the nuclear and cytoplasmic transcriptomes in iPSMNs carrying ALS-causing mutations in *TARDBP* and *VCP*, comparing them to iPSMNs from healthy controls (Figure 1A).[29,33,34] We analyzed 12 iPSMN lines, including four controls, two *TARDBP*^{G298S} mutants, two *VCP*^{R155C} mutants, two *VCP*^{R191Q} mutants, and two *VCP* R191Q mutant knockins introduced using CRISPR-Cas9 (Table S1A). For each line, we performed nuclear-cytoplasmic fractionation followed by extraction of RNA and protein. To examine the localization of transcripts, we performed deep RNA sequencing from nuclear and cytoplasmic fractions using poly(A) strand-specific sequencing, with an average of 189 million reads per sample (Table S1B; STAR Methods).

We confirmed high expression of neuronal markers across all iPSMNs (Figures 1B and 1C). To assess the quality of nucleocytoplasmic fractionation, we analyzed the proportion of sequencing reads aligning to exonic and intronic regions. Nuclear samples exhibited a higher proportion of intronic reads (mean nuclear 28.1%, cytoplasmic 9.4%) consistent with the presence of pre-mRNA transcripts. In contrast, cytoplasmic fractions were enriched with reads mapping to regions found in processed protein-coding mRNAs (5′ untranslated regions [UTRs], coding sequences [CDSs], and 3′ UTRs; mean nuclear 67.5%, cytoplasmic 88.0%; Figure 1D).[27] We also examined a nucleocytoplasmic fractionation database of 4,284 transcripts known to be enriched in either the nuclear or cytoplasmic compartments in the human cortex.[35] This demonstrated an increased abundance of the corresponding transcripts in their respective compartments in all iPSMN fractions (nuclear transcripts normalized enrichment score [NES] +2.7, $p < 1 \times 10^{-50}$; cytoplasmic transcripts NES +3.4, $p < 1 \times 10^{-50}$; Figures 1E and 1F). We visually confirmed the localization of individual transcripts known to reside in specific compartments using the genome browser, such as nuclear *MALAT1* and cytoplasmic *GAPDH* (Figure 1G). Principal component (PC) analysis and unsupervized hierarchical clustering showed sample separation based on subcellular fraction along PC1 and cell line along PC2 (Figure 1H). PC gene loadings indicated that PC1 separation was driven by nuclear and cytoplasmic marker genes (Figure S1A). To assess the quality of nucleocytoplasmic fractionation at the protein level, we employed western blot and mass spectrometry, confirming enrichment of nuclear and cytoplasmic marker proteins in their respective fractions (Figures S1B–S1E). Thus, our fractionated iPSMN model faithfully recapitulates fraction-specific mRNA and protein profiles, facilitating detailed investigation of ALS mutation effects on nucleocytoplasmic transcript and protein distribution.

Redistribution of the nucleocytoplasmic mRNA landscape in ALS iPSMNs

To quantify the nucleocytoplasmic distribution of transcripts in ALS iPSMNs, we developed a measurement that compares the nuclear/cytoplasmic mRNA ratios between ALS mutants and controls. We utilized a DESeq2 design that accounts for the pairing of nuclear and cytoplasm samples and tests for fraction and mutation effects. In *TARDBP*^{G298S} mutant iPSMNs, 381 transcripts were significantly redistributed (false discovery rate [FDR] < 0.05), with 153 redistributed to the nucleus and 228 to the cytoplasm (Figure 2A; Table S2). Eight of the redistributed transcripts encode known ALS genes, including *NEFL* (encodes neurofilament light), *ATXN1*, *HNRNPA2B1*, *ELP3*, and *MATR3*, while 46 encode other RBPs (e.g., *SRSF5*, *SRSF10*, *SNRNP200*, *ELAVL2*, and *POLDIP3*), and 10 encode nuclear export factors (e.g., *UPF1*, *SETD2*, and *CCHCR1*). Functional enrichment analysis revealed that both nuclear and cytoplasmic redistributed transcripts were independently enriched in protein binding and protein metabolism terms (Figure 2F).

In *VCP*^{R155C} mutant iPSMNs, 358 transcripts were significantly redistributed, with 181 redistributed to the nucleus and 177 to the cytoplasm (Figure 2B; Table S2). Among these, seven encoded known ALS genes (e.g., *FUS*, *OPTN*, and *NEFL*), while 35 encoded RBPs (e.g., *SNRNP200*, *ANKHD1*, and *PCBP3*), and five encoded nuclear export factors (e.g., *ANKLE1*, *FYTTD1*, and *RGPD5*). Functional enrichment analysis indicated an overrepresentation of protein binding and neuronal functions (Figure 2G).

In *VCP*^{R191Q} mutant iPSMNs, 602 transcripts were significantly redistributed: 181 to the nucleus and 421 to the cytoplasm (Figure 2C; Table S2). Among these, nine encoded known ALS genes, including *C9orf72*, *EWSR1*, and *NEFL*, while 59 encoded

Figure 1. Characterization of iPSMN nuclear and cytoplasmic transcriptomes

(A) Schematic of the experimental setup, involving reprogramming of ALS mutant, knockins, and control fibroblasts into iPSCs, and differentiated into motor neurons (iPSMNs). Motor neurons underwent fractionation into nuclear and cytoplasmic compartments followed by RNA sequencing and mass spectrometry.

(B) Representative immunolabeled images of iPSMNs, showing motor-neuron-specific markers, SMI-32, ChAT, and βIII tubulin. Scale bar: 20 μm.

(C) Heatmap displaying normalized gene counts for astrocytes, endothelial cells, myeloid cells, oligodendrocytes, and motor neurons across all samples.

(D) Read distribution showing how mapped reads are distributed over genome features for cytoplasmic samples and nuclear samples.

(E) Heatmap showing normalized gene expression of nuclear and cytoplasmic markers from the human cortex transcriptome database from Price et al.[35] Red represents increased gene expression, while blue represents decreased gene expression relative to other samples for each gene.

(F) Density plot showing differential gene expression for cytoplasmic (blue) and nuclear (red) markers from Price et al.[35] of nuclear versus cytoplasmic fractions. The area to the right of the black dotted line indicates an increase in nuclear samples, and the area to the left indicates an increase in cytoplasmic samples. The red and blue dotted lines are the mean $\log_2$ fold changes in nuclear and cytoplasmic markers, respectively.

(G) Coverage tracks of *MALAT1* (nuclear marker) and *GAPDH* (cytoplasmic marker). Nuclear reads are shown going upwards in red and cytoplasmic reads are down going in blue for control iPSMNs.

(H) Principal-component analysis of iPSMN nuclear and cytoplasmic fractions, visualizing samples along the first two principal components. Samples are labeled according to their cell line and colored by their cell type (red, nuclear; blue, cytoplasm).

Please cite this article in press as: Ziff et al., Nucleocytoplasmic mRNA redistribution accompanies RNA binding protein mislocalization in ALS motor neurons and is restored by VCP ATPase inhibition, Neuron (2023), https://doi.org/10.1016/j.neuron.2023.06.019

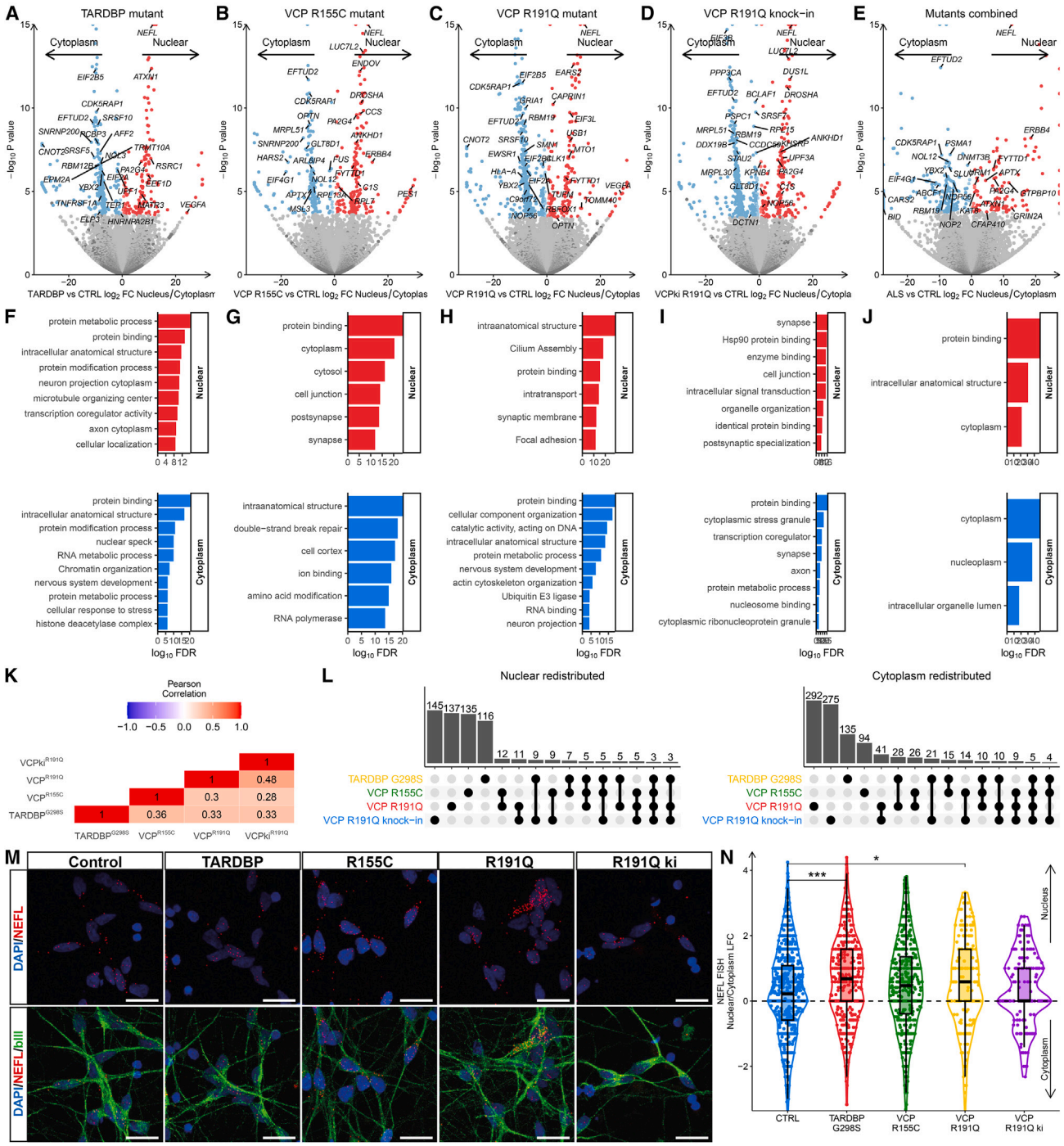

Figure 2. Nucleocytoplasmic transcript redistribution in *VCP* and *TARDBP* mutant iPSMNs

(A–E) Volcano plots showing nuclear/cytoplasm ratio changes in ALS versus control iPSMNs for (A) *TARDBP* mutant, (B) *VCP*^{R155C} mutant, (C) *VCP*^{R191Q} mutant, (D) *VCP*^{R191Q} knockin, and (E) mutants combined. Transcripts significantly redistributed to the nucleus are shown in red, and cytoplasmic redistributed transcripts are in blue.

(F–J) Bar graphs showing curated overrepresented functional categories of transcripts redistributed toward the nucleus (red) and cytoplasm (blue) for each mutant group.

(K) Heatmap showing the Pearson's correlation coefficient for transcriptome nucleocytoplasmic changes between each mutant group.

(L) UpSet plots showing the numbers of overlapping redistributed transcripts to the nucleus and cytoplasm between mutant groups.

(M) Representative images of fluorescence *in situ* hybridization (FISH) of *NEFL* transcript in iPSMNs. *NEFL* transcripts are shown in red, DAPI nuclear counterstain in blue, and βIII tubulin neuronal counterstain in green. Scale bar: 20 μm.

(legend continued on next page)

RBPs (e.g., *SRSF10*, *SMN1*, and *HNRNPD*), and 10 encoded nuclear export factors (e.g., *NUP98*, *RANBP1*, and *THOC2*). We identified functional enrichment of terms related to protein binding and neuronal structures (Figure 2H).

In VCP^{R191Q} knockin iPSMNs, 569 transcripts were significantly redistributed, with 190 redistributed to the nucleus and 379 to the cytoplasm (Figure 2D; Table S2). Among these, seven were in known ALS genes, including *NEFL*, while 76 belonged to RBPs (e.g., *SRSF7*, *SRSF2*, and *HNRNPK*), and 12 encoded nuclear export factors (e.g., *KPNB1*, *NUP88*, and *THOC6*). Functional enrichment analysis again revealed enrichment of protein binding and neuronal functions (Figure 2I).

We compared the nucleocytoplasmic mRNA redistribution between the ALS mutations. Correlation of transcriptome-wide nucleocytoplasmic changes revealed moderate positive associations with the strongest correlation observed between VCP^{R191Q} mutants and VCP^{R191Q} knockins (R = +0.48). VCP^{R155C} and VCP^{R191Q} mutants were also reasonably well correlated (R = +0.3) as was $TARDBP^{G298S}$ with VCP^{R191Q} (R = +0.33), VCP^{R155C} (R = +0.36), and VCP^{R191Q} knockin (R = +0.33; Figure 2I). Intersecting the redistributed transcripts between mutants confirmed an overlap greater than expected by chance for both nuclear and cytoplasm redistributed transcripts (all pairwise overlap Fisher tests $p < 1 \times 10^{-29}$; Figures 2K–2L). Across all four mutant groups, we identified three transcripts that were consistently nuclear redistributed and five that were consistently cytoplasmically redistributed. Among these were three RBPs (*EFTUD2*, *NOL12*, and *EZH2*) and *NEFL*, which encodes neurofilament light (NfL), an established ALS biomarker. These findings indicate that ALS mutations induce notable changes in transcript nucleocytoplasmic distribution, which is remarkably consistent across mutations.

To enhance statistical power in detecting redistribution across the four ALS mutant groups, we performed a combined mutant analysis (eight mutant lines versus four control lines). This revealed 330 significantly redistributed transcripts, with 134 redistributed to the nucleus and 196 to the cytoplasm (Figure 2E; Table S3). Among these, seven encoded known ALS genes (e.g., *NEFL*, *NOP56*, and *ATXN1*), while 36 encoded RBPs, and eight encoded nuclear export factors. Enrichment analysis confirmed that redistributed transcripts were enriched in protein binding and cell structure (Figure 2J). Considering the substantial transcript redistribution in ALS iPSMNs, we examined the expression of genes involved in nuclear mRNA export and the NPC at the whole-cell level. This revealed strong downregulation of NPC genes across all four mutant groups, particularly evident in *MX2, POM121B*, and *NXF5* (Figure S2).

To validate the nuclear accumulation of *NEFL* mRNA observed via RNA sequencing, we performed fluorescence *in situ* hybridization (FISH) specifically targeting the *NEFL* transcript (Figure 2M). This corroborated the nuclear accumulation of *NEFL* transcripts in $TARDBP^{G298S}$ (p = 0.0002), VCP^{R155C} (p = 0.29), VCP^{R191Q} (p = 0.03), and VCP^{R191Q} knockin (p = 1; Figure 2N) iPSMNs.

To investigate whether the redistributed transcripts observed in iPSMNs show altered expression in postmortem ALS tissue, we analyzed RNA sequencing from 271 postmortem spinal cord samples (ALS n = 214, CTRL n = 57) from the New York Genome Center (NYGC) ALS cohort.[36,37] Of the 330 redistributed transcripts in ALS mutant iPSMNs (combined analysis), 43 (14.5%) showed altered expression in ALS postmortem spinal cord. Among these, 27 were upregulated and 16 were downregulated, including the RBPs *PA2G4*, *JAKMIP1*, *PSMA1*, and *RBM34* and the ALS-related gene *ERBB4* (Table S2). While the fractionation of transcript distribution between the nucleus and cytoplasm is not possible with unfractionated postmortem data, the overlap of transcripts suggests that the observed transcriptome redistribution in iPSMNs may extend to global transcript expression in postmortem tissue.

Redistributed mRNAs display longer lengths and enhanced protein interactions

The nucleocytoplasmic localization of a transcript is influenced by its sequence features.[27] We compared the sequence features of redistributed transcripts to those of non-redistributed transcripts, including the total transcript length, the number of exons, and the lengths of the 5′ and 3′ UTRs. We observed that the average length of redistributed transcripts in all ALS mutant iPSMNs was approximately twice as long, with a significantly greater number of exons per transcript compared to non-redistributed mRNAs (Figures 3A, 3B, S3A, and S3B). Although there were no significant differences in 5′ UTR lengths, the 3′ UTRs of redistributed transcripts were longer compared to non-redistributed transcripts (Figures 3C and S3C–S3G).

mRNA localization is influenced by GC content and conserved localization signals.[38,39] Although no consistent association was found between GC content and redistributed transcripts, they showed trends toward higher conservation scores, indicating potential physiological roles for their nucleocytoplasmic shifts (Figures S3H and S3I). This suggests that longer, evolutionarily conserved mRNAs with more exons and longer 3′ UTRs are more prone to nucleocytoplasmic redistribution in ALS iPSMNs.

RBPs regulate splicing, transport, stability, and localization of mRNA. The altered mRNA localization observed in ALS iPSMNs may be linked to RBP mislocalization. We utilized the RNAct protein-RNA interactome database to assess predicted binding of redistributed mRNAs to proteins.[40] We examined the protein binding profile of each redistributed transcript from an "RNA-centric" view. This revealed significantly greater protein interaction scores for both nuclear and cytoplasmic redistributed transcripts compared to non-redistributed transcripts in all four mutant groups (Figure 3D; Table S3A). Interestingly, *GTPBP3*, *TMCO6*, and *U2AF1*, which encode RBPs themselves, were among the redistributed transcripts with the most abundant interactions with proteins. We validated these findings using crosslinking and immunoprecipitation (CLIP) data of 124 RBPs,

(N) *NEFL* transcript quantification by FISH showing the log fold change in the nuclear/cytoplasmic *NEFL* transcript ratio. CTRL cells n = 867, *TARDBP* n = 424, VCP^{R155C} n = 419, VCP^{R191Q} n = 189, and VCP^{R191Q} knockin n = 152. Wilcoxon test was used to determine significance (****p < 0.0001, ***p < 0.001, **p < 0.01, *p < 0.05).

Please cite this article in press as: Ziff et al., Nucleocytoplasmic mRNA redistribution accompanies RNA binding protein mislocalization in ALS motor neurons and is restored by VCP ATPase inhibition, Neuron (2023), https://doi.org/10.1016/j.neuron.2023.06.019

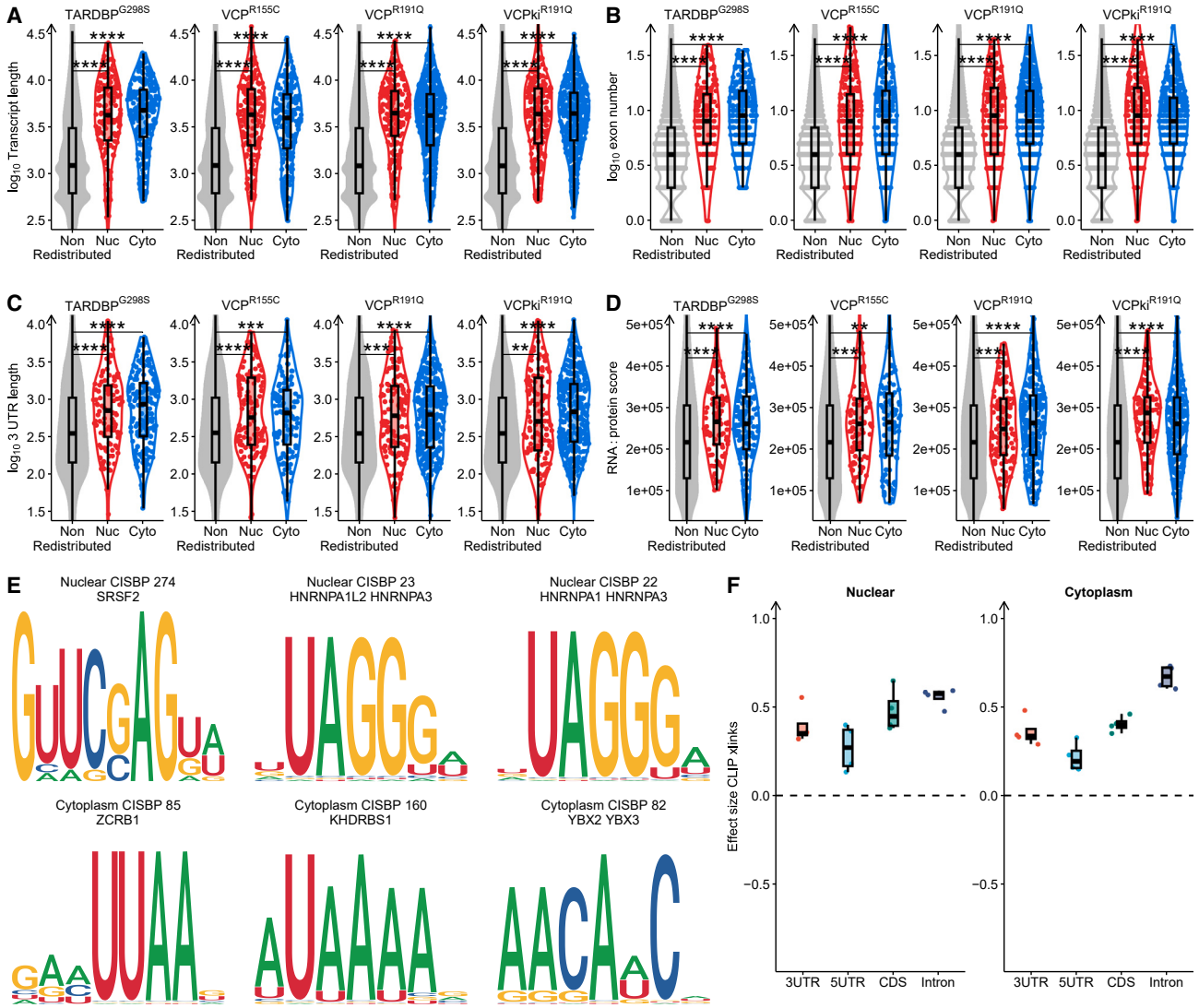

Figure 3. Features of nucleocytoplasmic redistributed transcripts in ALS iPSMNs

(A–D) Violin plots comparing nuclear (red), cytoplasmic (blue), and non-redistributed (gray) transcripts for (A) $\log_{10}$ transcript length, (B) $\log_{10}$ transcript exon count, (C) $\log_{10}$ 3′ UTR length, and (D) interaction score between each transcript with proteins (RNA view). Wilcoxon test was used to determine significance (****$p < 0.0001$, ***$p < 0.001$, **$p < 0.01$, *$p < 0.05$).

(E) The top enriched motif in nuclear redistributed transcripts (top) and cytoplasmic (bottom) across *TARDBP*^{G298S}, *VCP*^{R155C}, *VCP*^{R191Q}, and *VCP*^{R191Q} knockin iPSMNs.

(F) Cohen's D effect sizes comparing the enrichment of CLIP crosslinks in redistributed with non-redistributed transcripts in each transcript region. The dotted line represents no difference in crosslinks between redistributed and non-redistributed transcripts. The area above the dotted line indicates increased crosslinks to redistributed transcripts. Each dot represents a mutation group.

which confirmed higher enrichment of RBP binding in both nuclear and cytoplasmic redistributed transcripts compared with non-redistributed transcripts in all four mutant groups (Figure S3J).

Assessing protein-RNA interactions from the protein-centric viewpoint, we found that TDP-43 and FUS exhibited significantly greater interactions with both nuclear and cytoplasmic redistributed transcripts compared with non-redistributed transcripts (Figures S4A and S4B; Table S3B). Immunofluorescence analysis confirmed a significant decrease in the nucleocytoplasmic ratio of TDP-43 and FUS in the four mutant groups, suggesting that the cytoplasmic mislocalization of these ALS-related RBPs may contribute to transcript redistribution, or vice versa (Figures S5A and S5D). Furthermore, other RBPs implicated in ALS, such as *SFPQ*, *HNRNPA1*, *ATXN2*, *MATR3*, *HNRNPA2B1*, *TAF15*, *EWSR1*, and *ELAVL3*, consistently demonstrated greater interactions with redistributed transcripts compared with non-redistributed transcripts (Figures S4C–S4J).

We investigated whether specific RBP binding site motifs are overrepresented among redistributed transcripts. We examined

Please cite this article in press as: Ziff et al., Nucleocytoplasmic mRNA redistribution accompanies RNA binding protein mislocalization in ALS motor neurons and is restored by VCP ATPase inhibition, Neuron (2023), https://doi.org/10.1016/j.neuron.2023.06.019

CellPress
OPEN ACCESS

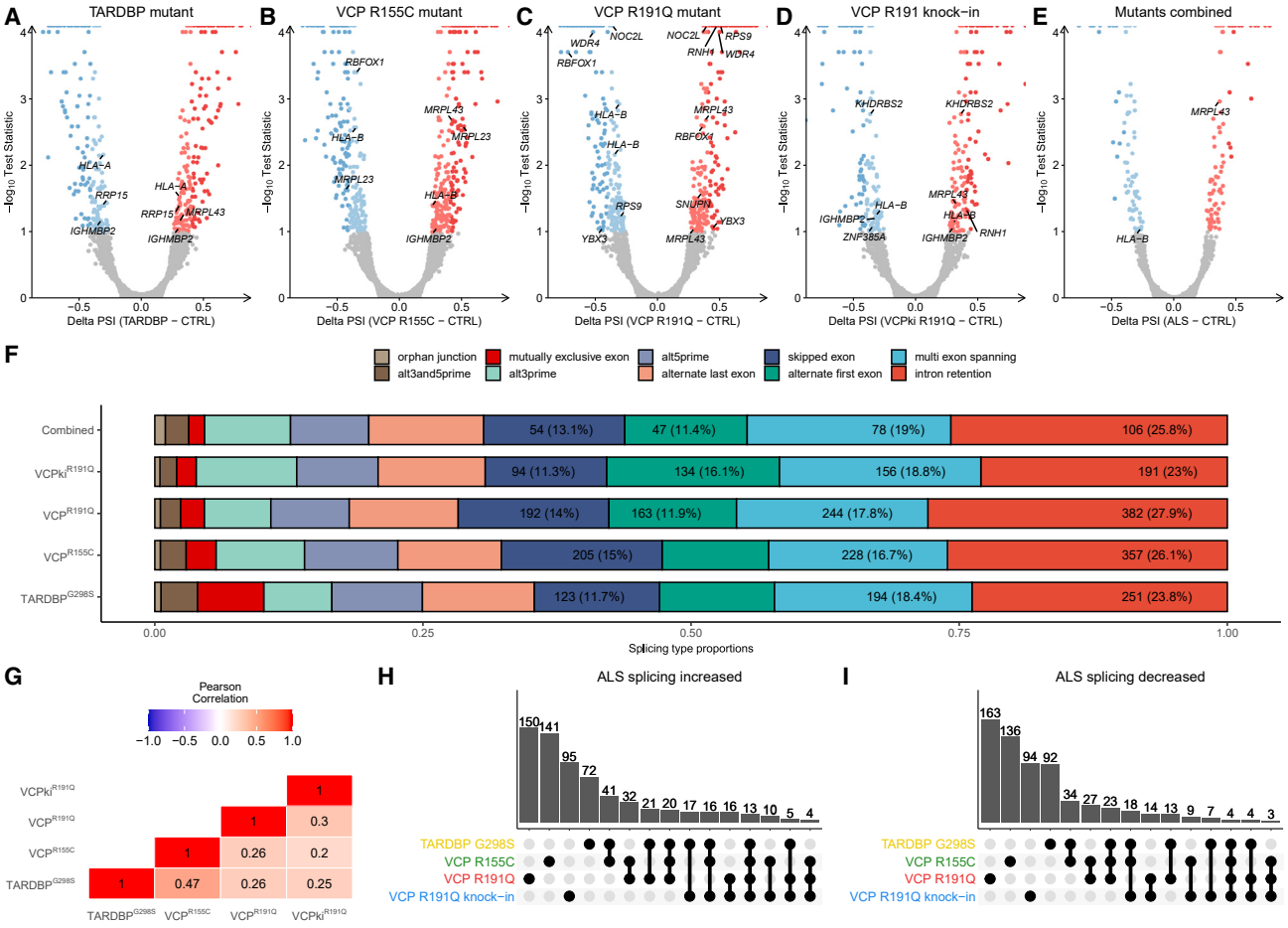

Figure 4. Splicing alterations in ALS iPSMNs

(A–E) Volcano plots showing splicing changes in ALS versus control whole-cell iPSMNs for (A) *TARDBP* mutant, (B) *VCP*^{R155C} mutant, (C) *VCP*^{R191Q} mutant, (D) *VCP*^{R191Q} knockins, and (E) mutants combined. Splice events that were significantly changed are colored red (increased in ALS) and blue (decreased).

(F) Bar chart showing proportions of each splicing type in significant splice events in each mutant group. Labels depict the numbers and percent of splice events for the splicing types (shown for those with >10%).

(G) Heatmap showing the Pearson's correlation coefficient for transcriptome splicing changes between each mutant group. All correlations have $p < 2.2 \times 10^{-16}$.

(H and I) UpSet plots showing the numbers of overlapping splice events (H) increased and (I) decreased between mutant groups.

motifs in the RBPDB and CISBP-RNA databases, encompassing 174 sequence motifs corresponding to 142 RBPs in the redistributed transcript groups.[41,42] Scanning the mRNA sequence of each redistributed transcript revealed that in *TARDBP*^{G298S} mutants, there were nine motifs significantly enriched in nuclear and seven in cytoplasmic redistributed transcripts (Table S3C). Although there were no motifs significantly enriched in *VCP*^{R155C} mutants, *VCP*^{R191Q} mutants exhibited 64 in nuclear redistributed transcripts and 60 in cytoplasmic redistributed transcripts. Similarly, *VCP*^{R191Q} knockins showed 102 significant motifs in nuclear redistributed transcripts and 33 in cytoplasmic redistributed transcripts. Across mutant groups, the motifs most enriched in nuclear redistributed transcripts corresponded to splicing factors (CISBP 274: SRSF2, CISBP 23: HNRNPA1L2 and HNRNPA3, and CISBP 22: HNRNPA1 and HNRNPA3), whereas motifs most enriched in cytoplasmic redistributed transcripts were CISBP 85: ZCRB1, CISBP160: KHDRBS1, and CISBP82: YBX2 and YBX3 (Figure 3E). These findings suggest a possible link between nucleocytoplasmic mRNA redistribution and perturbed RNA-RBP binding in ALS motor neurons.

To investigate which region of redistributed transcripts were most susceptible to RBP binding, we examined how CLIP crosslink enrichment varied between 5′ UTRs, 3′ UTRs, introns, and CDSs. In each transcript region, we found that both nuclear and cytoplasmic redistributed transcripts displayed stronger RBP interactions than non-redistributed transcripts (Figures S6A–S6D). Intronic regions displayed the greatest increase in RBP binding, followed by CDSs, 3′ UTRs, and 5′ UTRs (Figure 3F).

Altered splicing is linked to redistribution of a subset of mRNAs in ALS iPSMNs

Given that nuclear export of mRNA is coupled to splicing, we examined splicing changes in ALS mutant versus control iPSMNs using the splice graph tool MAJIQ.[43] Comparing *TARDBP*^{G298S} mutants with control iPSMNs revealed 400

significantly different splice events in 153 genes (Δ percent spliced in, $\Psi > 0.2$ and probability changing > 90%), with a majority harboring intron retention (IR; 223/400, 55.8%; Figure 4A; Table S4A). *VCP*^{R155C} mutants had 531 significant splice events in 218 genes, with 61.6% exhibiting IR (327/531; Figure 4B). *VCP*^{R191Q} mutants showed 512 significant splice events in 199 genes, with 60.5% (310/512) including IR (Figure 4C). *VCP*^{R191Q} knockins displayed 329 significant splice events in 139 genes, with IR present in 55.6% (183/329; Figure 4D). Combining the mutant iPSMNs revealed 174 significant splicing changes in 81 genes, with 115 (66.1%) containing IR (Figure 4E). Breaking down each complex splice event into their component splice types confirmed that in each mutant group, IR was the most common splicing type, accounting for 23%–28% of all splicing events (Figure 4F).

Correlating transcriptome-wide splicing changes between the different ALS mutants revealed moderate positive associations (R range +0.2 to +0.47). The strongest correlation was between *VCP*^{R155C} and *TARDBP*^{G298S} ($R = +0.47$, $p < 2 \times 10^{-16}$), followed by *VCP*^{R191Q} and *VCP*^{R191Q} knockin ($R = +0.3$, $p < 2 \times 10^{-16}$; Figure 4F). Intersecting significant splice changes between the mutant groups revealed 13 increased and 4 decreased splice changes that were consistent among all four mutant groups (Figures 4G–4I). Notably, these included genes involved in nucleocytoplasmic localization, including the RBP *MRPL43*, the cytoplasmic protein sequestering chaperone *GET4*, and the nuclear envelope protein *SUN1*, which was also among the cytoplasmic redistributed transcripts.

We intersected redistributed transcripts with differentially spliced transcripts. In *TARDBP*^{G298S}, two transcripts (*ZNF562*, and *YBEY*) showed both redistribution and differential splicing (Fisher exact test $p = 0.2$). In *VCP*^{R155C}, we found eight nuclear and five cytoplasmic redistributed transcripts among differentially spliced transcripts ($p = 5.1 \times 10^{-6}$). *VCP*^{R191Q} mutants exhibited 14 nuclear and 13 cytoplasmic redistributed transcripts that also showed differentially splicing ($p = 4.6 \times 10^{-16}$), while *VCP*^{R191Q} knockins had one nuclear and four cytoplasmic redistributed transcripts with altered splicing ($p = 0.04$). Interestingly, several of these transcripts with altered splicing and redistribution were shared among mutant groups, with *YBEY* and *SNHG29* present in three mutants and *RBFOX1*, *VLDLR-AS1*, *TMEM191B*, *NRCAM*, and *TPD52L2* existing in two of the four mutant groups. These results suggest that ALS mutations can induce substantial changes in splicing, particularly in intron retention, which may contribute to a subset of mRNA redistribution events in ALS motor neurons.

To examine the localization of the differentially spliced transcripts in ALS iPSMNs, we examined alternative splicing in nuclear-cytoplasmic fractionated samples. This compartment-specific approach revealed a larger number of significant splicing changes compared with whole-cell iPSMNs (*TARDBP* 817, *VCP*^{R155C} 867, *VCP*^{R191Q} 2,170, *VCP*^{R191Q} knockin 2,429; Figure S6E).

When comparing nuclear and cytoplasmic fractions, we found more significant splicing changes in the nucleus than in the cytoplasm across all four mutants. Approximately a quarter of splicing changes were shared between the fractions: *TARDBP* (nuclear: 579, cytoplasm: 303, shared: 65), *VCP*^{R155C} (nuclear: 558, cytoplasm: 440, shared: 131), *VCP*^{R191Q} (nuclear: 1,585, cytoplasm: 774, shared: 189), and VCP^{R191Q} knockin (nuclear: 2,157, cytoplasm: 343, shared: 71; Table S4B). Interestingly, a significant number of redistributed transcripts were identified among these fraction-specific splicing events: *TARDBP* (8, Fisher $p = 0.003$), *VCP*^{R155C} (20, $p = 5.9 \times 10^{-13}$), *VCP*^{R191Q} (64, $p = 9 \times 10^{-36}$), and *VCP*^{R191Q} knockin (55, $p = 1 \times 10^{-24}$). Correlating splicing changes between nuclear and cytoplasmic fractions revealed moderate positive associations (*TARDBP*: $R = +0.26$, *VCP*^{R155C}: $R = +0.28$, *VCP*^{R191Q}: $R = +0.41$, *VCP*^{R191Q} knockin: $R = +0.34$; Figure S6F). Analysis of splicing types showed that nuclear fractions had a higher proportion of IR events (nuclear: 32%–52%, cytoplasm: 17%–26%), while cytoplasmic fractions exhibited more exon skipping and multi-exon spanning splicing changes, indicating that IR is linked to the nuclear detention of transcripts (Figure S6G). The distinct splicing changes observed in the nuclear and cytoplasmic fractions indicate that disruptions in splicing and transcript isoform switching may contribute to the redistribution of a subset of transcripts in ALS.

Proteomics reveals widespread mislocalization of RBPs in ALS iPSMNs

To assess how transcript redistribution relates to the nucleocytoplasmic mislocalization of proteins in ALS iPSMNs, we employed quantitative proteomics. We applied shotgun data-dependent analysis (DDA) mass spectrometry on triplicate sets of the same iPSMN cultures that underwent RNA sequencing. To define nucleocytoplasmic mislocalization of proteins in ALS iPSMNs, we utilized the same approach as for transcript redistribution, contrasting nuclear/cytoplasm ratios between ALS mutants and controls while accounting for nuclear-cytoplasm sample pairing using limma.[44]

In *TARDBP*^{G298S} mutant iPSMNs, we found 577 significant mislocalized proteins (FDR < 0.05), of which 169 (29.3%) mislocalized to the nucleus and 408 (70.7%) to the cytoplasm (Figure 5A; Table S5). 11 ALS-related proteins, including HNRNPA1, UNC13B, and FUS, were among those mislocalized together with 137 other RBPs (e.g., SRSF4, SRSF11, and UPF1) and 22 nuclear export factors (e.g., NUP155, NUP54, and NUP160). Functional enrichment analysis confirmed that mRNA binding and protein binding were overrepresented among nuclear and cytoplasmic mislocalized proteins (Figure 5B).

In *VCP*^{R155C} mutant iPSMNs, we identified 169 significant mislocalized proteins, of which 55 (32.5%) were shifted toward the nucleus and 114 (67.5%) toward the cytoplasm (Figure 5C; Table S5). The ALS-related RBPs FUS, NOL4L, and ELAVL3 were mislocalized to the cytoplasm along with 21 other RBPs (e.g., DDX6, RPP30, and LONP1) and 5 nuclear export factors (NUP62, RANBP1, NUP155, ALKBH5, and MAGOH). Nuclear mislocalized proteins were enriched in endoplasmic reticulum and Golgi transport while cytoplasmic mislocalized proteins were overrepresented by nucleocytoplasmic localization functions and protein binding (Figure 5D).

In *VCP*^{R191Q} mutant iPSMNs, we identified 867 significantly mislocalized proteins, with 754 (87%) of these mislocalized to the cytoplasm (Figure 5E; Table S5). Among mislocalized proteins were 5 ALS-related RBPs (FUS, HNRNPA1, HNRNPA2B1,

Please cite this article in press as: Ziff et al., Nucleocytoplasmic mRNA redistribution accompanies RNA binding protein mislocalization in ALS motor neurons and is restored by VCP ATPase inhibition, Neuron (2023), https://doi.org/10.1016/j.neuron.2023.06.019

CellPress
OPEN ACCESS

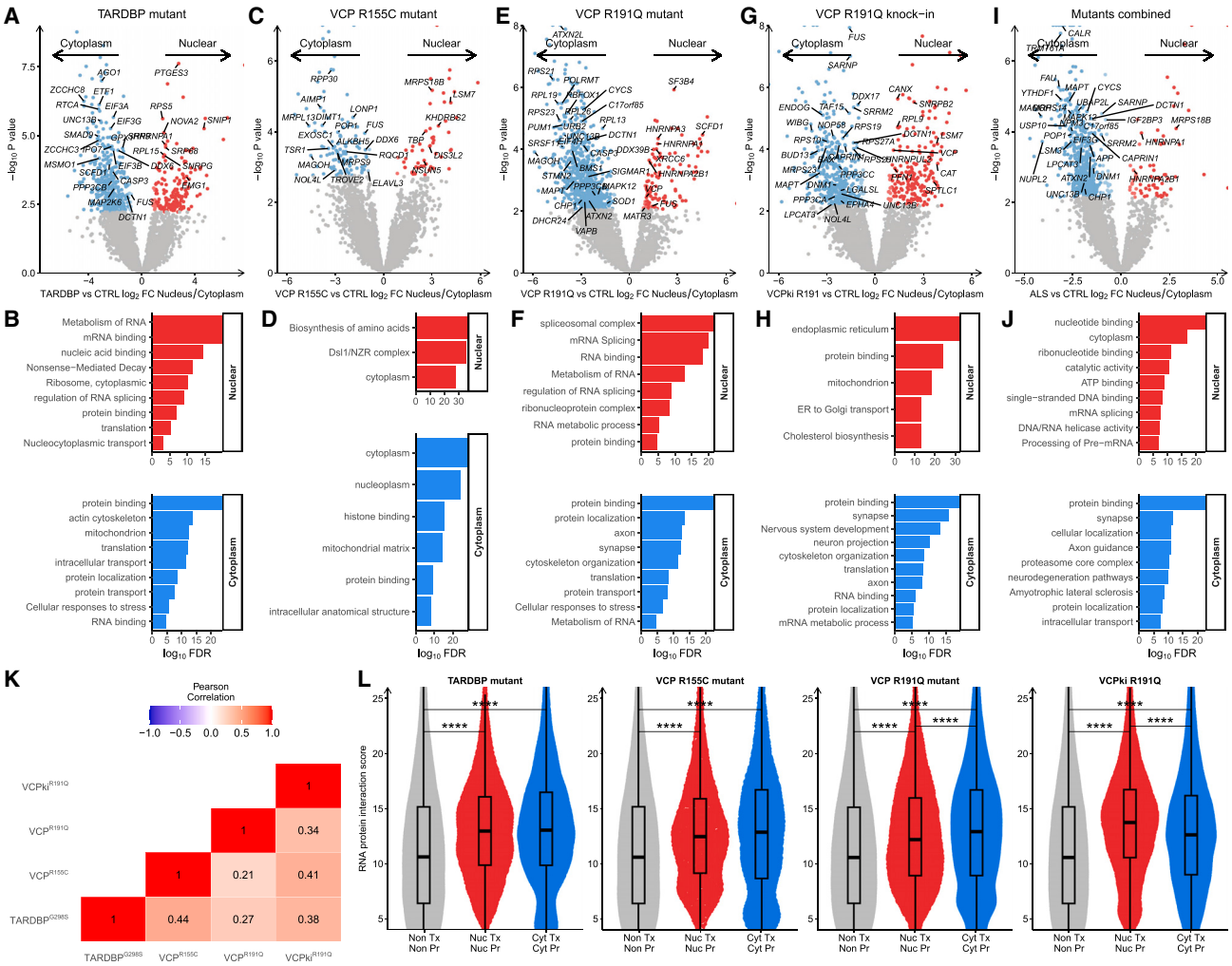

Figure 5. Nucleocytoplasmic protein mislocalization in ALS iPSMNs

(A, C, E, G, and I) Volcano plots showing nuclear/cytoplasm ratio changes in ALS versus control iPSMNs for (A) *TARDBP* mutant, (C) *VCP*^{R155C} mutant, (E) *VCP*^{R191Q} mutant, (G) *VCP*^{R155C} knockin, and (I) mutants combined. Significantly mislocalized proteins to the nucleus are shown in red, and cytoplasmic mislocalized proteins are in blue.

(B, D, F, H, and J) Bar graphs showing curated overrepresented functional categories of proteins mislocalized toward the nuclear (red) and cytoplasm (blue) for (B) *TARDBP* mutant, (D) *VCP*^{R155C} mutant, (F) *VCP*^{R191Q} mutant, (H) VCP^{R191Q} knockin, and (J) mutants combined.

(K) Heatmap showing the Pearson's correlation coefficient for proteome-wide nucleocytoplasmic changes between each mutant group.

(L) Violin plots showing RNAct transcript (Tx)-protein (Pr) interaction scores between non-redistributed transcripts and non-mislocalized proteins (gray), nuclear redistributed transcripts and nuclear mislocalized proteins (red), and cytoplasmic redistributed transcripts and cytoplasmic redistributed proteins (blue). t test was used to determine significance (****$p < 0.0001$, ***$p < 0.001$).

ATXN2, and MATR3), as well as 16 other ALS-related proteins (e.g., UNC13B, STMN2, VCP, and MAPT), 167 other RBPs (e.g., SRSF7, SRSF11, and HNRNPA3), and 31 nuclear export factors (e.g., THOC7, DDX39B, and KPNA1). Mislocalized proteins were enriched in RNA splicing, RNA binding, and protein binding functions (Figure 5F).

In *VCP*^{R191Q} knockin iPSMNs, we found 639 significant mislocalized proteins, of which two-thirds (436, 68.2%) were again mislocalized to the cytoplasm (Figure 5G; Table S5). Among mislocalized proteins were 17 ALS-related proteins (including TDP-43, FUS, and VCP), 120 other RBPs (e.g., HNRNPLL, DDX17, and TAF15), and 17 nuclear export factors (e.g., NUP62, NUP35, and ALYREF). Functional enrichment analysis revealed enrichment of endoplasmic reticulum, RNA metabolism, and protein binding functions (Figure 5H).

Comparing nucleocytoplasmic protein mislocalization between mutations revealed considerable proteome-wide positive relationships (range R = +0.23 to +0.44; Figures 5I and S7I–S7N), indicating global concordance in ALS protein mislocalization. Intersecting mislocalized proteins between the four mutant groups revealed two nuclear mislocalized (H3F3B and HIST1H2AJ) and 11 cytoplasmic mislocalized (including DYNLRB1, ATP6V0A1, SPAG9, UBXN4, and FUS; Figures S7O–S7P).

Please cite this article in press as: Ziff et al., Nucleocytoplasmic mRNA redistribution accompanies RNA binding protein mislocalization in ALS motor neurons and is restored by VCP ATPase inhibition, Neuron (2023), https://doi.org/10.1016/j.neuron.2023.06.019

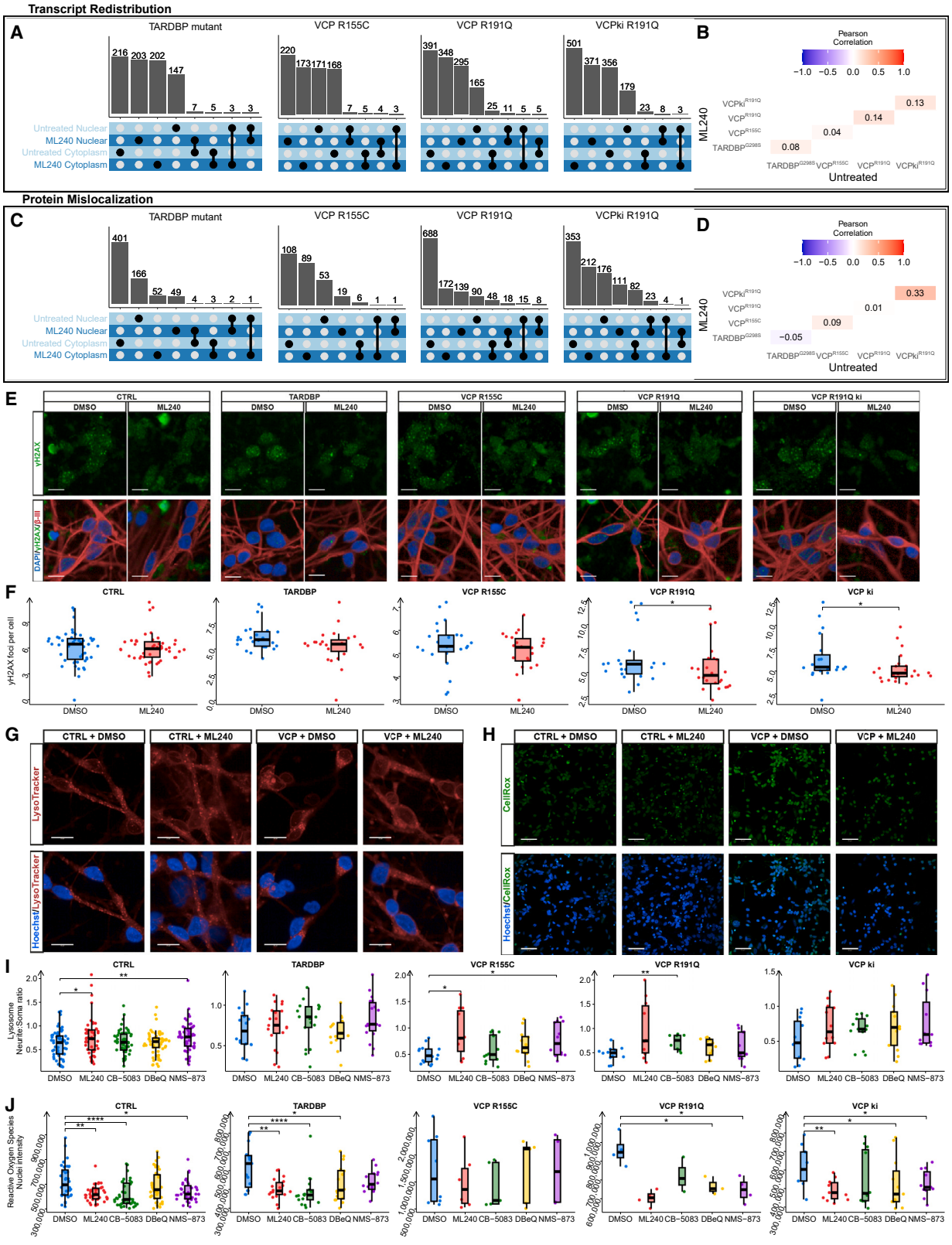

(legend on next page)

By combining mutants in an integrated analysis, we revealed 578 significant mislocalized proteins common across the four mutant groups. The vast majority of these were mislocalized to the cytoplasm (508, 87.9%; Figure 5I; Table S5). Among mislocalized proteins were 12 ALS-related proteins (including ATXN2, HNRNPA2B1, and UNCB13), 90 other RBPs, and 15 nuclear export factors (e.g., NUP155, NUP62, and HNRNPA1). Mislocalized proteins were enriched in functions related to RNA metabolism and protein processing (Figure 5J).

Despite the similarity between these functionally enriched terms with those enriched among redistributed transcripts, we found that mRNA nucleocytoplasmic redistribution was not correlated with protein nucleocytoplasmic mislocalization (all Pearson R = 0.0; Figures S7A–S7D) or whole-cell protein abundance changes in any mutant group (all R = 0.0; Figures S7E–S7H), consistent with previous reports comparing mRNA with protein changes.[17,31,45]

To determine whether the widespread nucleocytoplasmic mislocalization of proteins was related to altered expression of nuclear export proteins, we examined changes in the expression of nuclear mRNA export and the NPC proteins. This revealed many significant changes in the protein expression across nucleocytoplasmic transport domains, most notably in *TARDBP* (n = 311 differential nucleocytoplasmic transport proteins) and VCP^{R155C} mutants (n = 509; VCP^{R191Q} n = 37; VCP^{R191Q} knockin n = 58; Figure S8). This finding confirms altered expression of mRNA nuclear export factors, which may directly contribute to the mislocalization of transcripts and proteins.

To identify whether interactions between mRNAs and proteins contribute to their nucleocytoplasmic localization changes in ALS, we examined the predicted interactions between redistributed transcripts and mislocalized proteins. In each mutant group, we found significantly greater interaction scores between fraction-specific redistributed mRNAs and mislocalized proteins compared with the interaction scores between non-redistributed mRNAs and non-mislocalized proteins (Figure 5L). Comparing interactions between redistributed transcripts and mislocalized proteins in the nucleus and the cytoplasm revealed consistently greater interactions between cytoplasmic shifted transcripts and proteins than between nuclear shifted transcripts and proteins. Across mutant groups, mislocalized proteins with the greatest binding to cytoplasmic redistributed transcripts were SPAG9, ATP6V0A1, and ADD2, while ANP32E, CLTA, and PPP1R14B showed the greatest binding to nuclear redistributed transcripts (Table S6A). From the RNA view, redistributed transcripts with the greatest binding scores to mislocalized proteins were WDR86, SLC22A17, and CADM1 (Table S6B). These data support the concept that interactions between mRNA and proteins contribute to widespread nucleocytoplasmic redistribution and mislocalization in ALS motor neurons.

VCP ATPase inhibition partially restores transcript redistribution, splicing, and protein mislocalization

VCP inhibition reduces the excessive ATPase activity and cofactor interactions associated with *VCP* mutations, leading to improvements in mitochondrial function and motor neuron survival.[46–54] To identify whether VCP inhibition can restore transcript redistribution and protein mislocalization in ALS motor neurons, we treated *VCP* and *TARDBP* mutant iPSMNs with ML240, an inhibitor targeting the VCP D2 ATPase domain.[55,56] We performed a cell viability assay and confirmed that ML240 treatment did not negatively impact the survival of iPSMNs (Figures S9A and S9B). We then subjected ML240-treated iPSMNs to subcellular fractionation and performed RNA sequencing and mass spectrometry (Figures S9C–S9H). Comparing the nuclear/cytoplasm ratios of untreated and ML240-treated control (non-mutant) cultures revealed strong correlations for both mRNA (R = +0.9) and protein (R = +0.78; Figures S10A and S10B), indicating that ML240 treatment has modest effects on the transcriptome and proteome in control cultures.

In ALS mutant iPSMNs treated with ML240, we observed similar numbers of redistributed transcripts compared with their untreated counterparts (*TARDBP* ML240 n = 423 vs. untreated n = 381; VCP^{R155C} 412 vs. 358, VCP^{R191Q} 689 vs. 602, VCP^{R191Q} knockin 906 vs. 569; Figures S10C–S10G). However, the identities of the redistributed transcripts changed substantially upon ML240 treatment. In *TARDBP* mutants, only 3 out of 153 nuclear redistributed transcripts and 5 out of 228 cytoplasmic redistributed transcripts remained after ML240 treatment (98% rescued; Figures 6A and S10; Table S2). In VCP^{R155C} mutants, after ML240, only 7 of 181 nuclear redistributed transcripts remained (96.1% rescued) and 5 of 177 cytoplasmic redistributed transcripts remained (97.2% rescued). In VCP^{R191Q} mutants, ML240 corrected nuclear redistributed transcripts by 93.9% (11 of 181 remained) and cytoplasmic redistributed transcripts by 94.1% (25 of 421 remained). In VCP^{R191Q} knockins, ML240 treatment reversed nuclear redistributed transcripts by 95.8% (8 of 190 remained) and cytoplasmic redistributed transcripts

Figure 6. VCP ATPase inhibition restored mRNA and protein localization in ALS iPSMNs

(A) UpSet plot showing the numbers of overlapping redistributed transcripts to the nucleus and cytoplasm in untreated and ML240-treated conditions in $TARDBP^{G298S}$, VCP^{R155C}, VCP^{R191Q}, and VCP^{R191Q} knockin iPSMNs.

(B) Heatmap showing the Pearson correlation of nucleocytoplasmic transcriptome redistribution in untreated (x axis) against ML240-treated (y axis) redistribution in each mutant group.

(C and D) UpSet plot and correlation heatmap as for (A) and (B) but showing protein mislocalization rather than transcript redistribution.

(E and F) Number of γH2AX nuclear foci in CTRL, $TARDBP^{G298S}$, VCP^{R155C}, VCP^{R191Q}, and VCP^{R191Q} knockin iPSMNs with representative images in (E) and quantifications in (F). Data from six independent experimental repeats. Scale bar: 10 μm.

(G and H) LysoTracker lysosome (G) and CellROX oxidative stress (H) assays in CTRL and *VCP* mutant iPSMNs, with ML240 treatment or DMSO. Scale bar in (G): 20 μm. Scale bar in (H): 50 μm.

(I and J) Quantifications of the ratio of lysosomes in the neurites to soma (I) and nuclear CellROX intensity (J) in each mutant group with DMSO (blue) and VCP inhibitors (ML240, red; CB-5083, green; DBeQ, yellow; and NMS-873, purple). Data from at least three independent experimental repeats. Wilcoxon test was used to determine significance (****$p < 0.001$, **$p < 0.1$, *$p < 0.05$).

by 93.9% (23 of 379 remained). Intersecting transcripts that remain redistributed between mutant groups revealed five transcripts shared between two mutant groups (*GDI1*, *SPAST*, *IBTK*, *DPYSL5*, and *SNHG11*; Table S7A).

Comparing ML240 with untreated samples revealed very weak correlations in nucleocytoplasmic changes for each ALS mutant group (*TARDBP* R = +0.08, VCP^{R155C} R = +0.04, VCP^{R191Q} R = +0.14, VCP^{R191Q} knockin R = +0.13; Figure 6B), indicating that ML240 exerts substantial changes in the nucleocytoplasmic distribution of mRNA in ALS iPSMNs. Functional enrichment analysis showed that although protein binding remained overrepresented, ATP binding was newly enriched (Figures S10H–S10K). Redistributed transcripts that were rescued by ML240 were enriched in protein metabolism, neuronal components, and the stress response (Figures S10L–S10O).

ML240 treatment rescued splicing changes in ALS mutant iPSMNs, with a large proportion of altered splice events being reversed (*TARDBP* 66.3%, 135 of 400; VCP^{R155C} 53.9%, 245 of 531 remained; VCP^{R191Q} 53.1%, 240 of 512; VCP^{R191Q} knockins 65.3% 114 of 329; Figure S11A; Table S7B). ML240-treated samples also showed weak-moderate correlations with untreated samples (*TARDBP* R = +0.25, VCP^{R155C} R = +0.36, VCP^{R191Q} R = +0.41, and VCP^{R191Q} knockin R = +0.29; Figure S11B). Examining the types of splicing revealed that ML240-treated samples showed similar proportions of each splicing type as their untreated counterparts (Figure S11C). The rescue of most splicing changes by ML240 suggests that splicing modification could potentially contribute to the indirect effect of ML240 on nucleocytoplasmic transcript redistribution.

We next quantified the effect of ML240 on the mislocalization of proteins in ALS iPSMNs. For each mutant group, we found substantially fewer mislocalized proteins with ML240 treatment compared to untreated iPSMNs: *TARDBP* mutants 81% reduction (ML240 n = 111 vs. untreated n = 577), VCP^{R155C} 31% reduction (ML240 116 vs. untreated 169), VCP^{R191Q} 54% reduction (ML240 400 vs. untreated 867), VCP^{R191Q} knockin 32% reduction (ML240 433 vs. untreated 639; Figures S12A–S12E; Table S7C). In *TARDBP* mutants, ML240 reversed 99% of both nuclear (167 of 169) and cytoplasmic (405 of 408) mislocalized proteins compared to untreated samples (Figure 6C). In VCP^{R155C} mutants, ML240 corrected 98% of nuclear (1 of 55 remained) and 95% of cytoplasmic (6 of 114 remained) mislocalized proteins. In VCP^{R191Q} mutants, 93% (8 of 113 remained) of nuclear and 94% (48 of 754 remained) of cytoplasmic mislocalized proteins were rectified. In VCP^{R191Q} knockins, 89% (23 of 203 remained) of nuclear and 81% (82 of 436 remained) of cytoplasmic mislocalized proteins were rescued.

Comparing nucleocytoplasmic changes in the proteome between ML240-treated and untreated iPSMNs revealed weak correlations in *TARDBP* mutant (R = −0.05), VCP^{R155C} (R = +0.08), VCP^{R191Q} (R = +0.01), and VCP^{R191Q} knockin (R = +0.32; Figure 6D), consistent with ML240 exerting considerable changes on protein localization in ALS iPSMNs. Functional enrichment analysis of mislocalized proteins after ML240 treatment showed the persistence of protein binding and splicing functions but also newly enriched pathways related to lipid and mitochondrial metabolism (Figures S12F–S12I). Mislocalized proteins that were rescued by ML240 were enriched in RNA and protein metabolism, as well as cellular transport functions (Figures S12J–S12M), indicating that the normalization of nucleocytoplasmic transport mechanisms may contribute to the reversal of mislocalization with ML240.

Interactions between mRNAs and proteins with ML240 treatment remained greater between redistributed mRNAs and mislocalized proteins compared to interactions between non-redistributed mRNAs and non-mislocalized proteins (Figure S12M). This suggests that mRNA-protein interactions play a role in determining their localization changes irrespective of VCP ATPase inhibition. Taken together, these findings demonstrate that ML240 can restore alterations in the transcriptome and proteome not only in the context of *VCP* mutations but also in *TARDBP* mutations.

ML240 alters interactions between VCP and nucleocytoplasmic transport proteins

To investigate the effects of VCP ATPase inhibition on VCP protein binding interactions, we performed VCP immunoprecipitation in iPSMNs before and after ML240 treatment. This enabled us to isolate VCP protein complexes and identify the proteins that interact with VCP using mass spectrometry (Figure S13A). In untreated control iPSMNs, we detected 4,479 proteins that interact with VCP, including TDP-43 and FUS. By comparing untreated iPSMNs with ML240-treated iPSMNs, we investigated the impact of ML240 on the VCP protein interactome. In control iPSMNs, we observed large shifts in VCP binding partners following ML240 treatment, with 165 protein interactions significantly increased and 337 significantly decreased (Figure S13B; Table S8). Functional enrichment analysis of these altered interactions revealed enrichment in RNA and protein metabolism and nucleocytoplasmic localization functions, supporting the hypothesis that VCP interacts with proteins that regulate nucleocytoplasmic RNA and protein distribution (Figure S13G). Among downregulated terms we identified VCP AAA ATPase complex (VCP, FAF2, NPLOC4), indicating an on-target effect of ML240 on the VCP protein.

We next examined how ML240 affects the VCP interactome in ALS mutant iPSMNs. Although there were no significantly changed VCP binding partners in *TARDBP* mutants, in VCP^{R155C} mutants 78 proteins showed increased interactions and 64 decreased with ML240. VCP^{R191Q} mutants showed 37 increased and 13 decreased interactions; and VCP^{R191Q} knockins showed 23 increased and 87 decreased interactions (Figures S13C–S13F; Table S8). These changes in VCP interactions with ML240 were associated with nucleocytoplasmic transport, RNA metabolism and protein binding functions. Thus, ML240 affects the VCP interactome, potentially contributing to the restoration of the distribution of RNA and proteins in ALS mutant iPSMNs (Figures S13G–S13J). ML240 showed moderate positive correlations in altering the VCP interactome across control and mutant iPSMN groups (R = +0.25 to +0.46; Figure S13K). There were common protein targets affected by ML240 in *VCP* mutant groups, including RAE1, HMGB1, PAE1, RPL10, and HSP90AB2P (Figures S13L–S13M). Intersecting proteins altered in their VCP interactions by ML240 with rescued mislocalized proteins revealed significant overlaps in both VCP^{R155C} mutants (Fisher p = 0.007, 11 of 142) and VCP^{R191Q} knockins (p = 0.02, 18

of 101; *TARDBP* 0 of 567; *VCP*^{R191Q} mutant p = 0.8, 6 of 50). These findings support the idea that ML240-induced reconfiguration of the VCP interactome in *VCP* mutant iPSMNs contributes to the restoration of nucleocytoplasmic transcript and protein mislocalization.

VCP ATPase inhibition is associated with improved ALS phenotypes

We investigated whether VCP ATPase inhibition is associated with improved ALS-related iPSMN phenotypes. We used the γH2AX assay to assess DNA damage and found that ML240 consistently reduced γH2AX nuclear foci in both ALS mutant and control cultures, suggestive of reduced DNA damage (Wilcoxon p values CTRL 0.2, *TARDBP* 0.7, *VCP*^{R155C} 0.2, *VCP*^{R191Q} 0.03, *VCP*^{R191} knockin 0.01; Figures 6E and 6F). We used LysoTracker to examine lysosome localization and function. ML240 caused lysosomes to shift from the soma to neurites in all cultures (Wilcoxon p values CTRL 0.03, *TARDBP* 0.5, *VCP*^{R155C} 0.01, *VCP*^{R191Q} 0.07, *VCP*^{R191} knockin 0.2; Figures 6G–6I and S13N). This trend was also observed with three other VCP inhibitors: CB-5083 (a more specific derivative of ML240 that reversibly competes for the ATPase domain), DBeQ (reversible competitive antagonist of ATP at both the D1 and D2 domains), and NMS-873 (reversible allosteric inhibitor binding to the D2 domain).[57] These findings indicate that VCP inhibition, regardless of the specific inhibitor used, leads to restoration of neurite-localized endo-lysosomal function.

Since oxidative stress contributes to ALS pathogenesis and has been found in our *VCP* mutant iPSMN cultures,[29] we examined levels of intracellular reactive oxygen species (ROS; Figure 6H). Basal levels of ROS were increased in *VCP*^{R155C} and *VCP*^{R191Q} mutant groups compared to control iPSMNs (Wilcoxon p = 0.0001 and p = 0.00003, respectively; Figure S13O). However, ML240 treatment consistently reduced ROS in all mutant groups as well as control iPSMNs (p values *TARDBP* 0.003, *VCP*^{R155C} 0.4, *VCP*^{R191Q} 0.09, *VCP*^{R191Q} knockin 0.003, control 0.01; Figure 6J). Similarly, the three other VCP inhibitors (CB-5083, DBeQ, and NMS-873) also led to consistent reductions in ROS levels. These findings indicate that VCP inhibitors have the potential to partially reverse ALS-related phenotypes in iPSMNs, as demonstrated by the reduction in γH2AX nuclear foci, the shift of lysosomes to neurites, and the decrease in ROS levels.

DISCUSSION

The question of whether mRNA redistribution accompanies RBP mislocalization in ALS has been relatively neglected. Defects in nucleocytoplasmic transport have been increasingly implicated in ALS, and mutations in mRNA export factors such as *ALYREF*, *MATR3*, and *GLE* have been causally linked to ALS.[10–12,15,58] Moreover, components of the nucleocytoplasmic transport machinery and nuclear export factors, including nucleoporins and karyopherins, can be sequestered by cytoplasmic protein aggregates.[10–12,14,59,60] Our study revealed numerous NPC components, mRNA export factors, and other RBPs among the redistributed transcripts and mislocalized proteins. Furthermore, faulty nucleocytoplasmic transport is supported by our finding that longer transcripts are more prone to redistribution, as smaller transcripts can more readily traverse the NPC.[61,62] However, the altered nucleocytoplasmic localization of longer transcripts, which possess more introns, could also signify defective RNA processing.[63] Additionally, longer transcripts offer a larger binding surface for mRNA export complexes and other RBPs, rendering them potentially more susceptible to processing defects that impede correct localization.[27] TDP-43 and FUS preferentially influence the splicing of lengthy transcripts with neuronal functions, and their mislocalization may render these transcripts more vulnerable to mis-splicing and redistribution in ALS.[64] Our findings provide support for the hypothesis that RNA processing and interactions with RBPs are fundamental to mRNA redistribution, as we observed an enrichment of redistributed transcripts with longer 3′ UTRs, RBP interactions, and splicing defects.[65–67]

The localization of RBPs can be influenced by the relative RNA content between the nucleus and the cytoplasm. A recent study found that cytoplasmic RNA decay mediated by RNase-L triggers the relocalization of RBPs toward the nucleus. This relocalization is attributed to the comparatively longer persistence of nuclear RNA, affecting RNA splicing within the nucleus. Thus, the distribution of RBPs between the nucleus and cytoplasm is contingent upon the availability of RNA in each compartment.[68] Additionally, inhibiting transcription has been observed to accelerate the nuclear export of TDP-43, suggesting that newly synthesized RNA helps in retaining TDP-43 in the nucleus.[69]

A prominent finding among the ALS mutations studied was the nuclear accumulation of NEFL mRNA, which encodes the NfL protein. This is interesting because NfL is a recognized biomarker for axonal degeneration.[70] Normally, nuclear TDP-43 interacts with the NEFL 3′ UTR, stabilizing NEFL mRNA. In ALS, TDP-43 mislocalization may contribute to impaired NEFL splicing and stability.[71–73] We speculate that the nuclear accumulation of NEFL mRNA could be a compensatory mechanism where increased transcriptional synthesis helps counter the reduced stability of NEFL mRNA, maintaining normal cytoplasmic NEFL levels and sufficient translation into NfL protein. At the protein level, we observed a consistent non-significant trend of NfL shifting toward the cytoplasm in ALS iPSMNs. Many questions remain, such as whether the nucleocytoplasmic shifts of NEFL mRNA and NfL protein represent a protective or detrimental response and how they relate to NfL as a biomarker.

We observed extensive protein mislocalization in ALS iPSMNs, with two-thirds of the mislocalized proteins shifting toward the cytoplasm. We confirmed the nuclear-to-cytoplasmic mislocalization of FUS, as well as other RBPs associated with ALS, including *HNRNPA1* and *TAF15*.[74] These mislocalized proteins were enriched in RNA binding functions, supporting the concept of ALS as a multi-RBP-opathy. Importantly, we also discovered enhanced predicted interactions between mislocalized proteins and redistributed transcripts, providing further evidence for the involvement of RBP mislocalization in mRNA redistribution.[8] This holds pathological implications in ALS, as nucleocytoplasmic shifts in ribonucleoprotein complexes disrupt liquid-liquid phase separation dynamics and potentially contribute to the formation of insoluble aggregates.[75–77]

Considering the functional consequences of an environment prone to aggregation, restoring nucleocytoplasmic homeostasis of mRNA and RBPs is a promising therapeutic strategy in ALS.

Abnormal VCP ATPase activity in ALS disrupts the diverse functions of VCP, which may contribute to the mislocalization of aggregation-prone RBPs and redistribution of their bound mRNAs.[46–51,78] A noteworthy finding in our study was the effectiveness of ML240, an inhibitor of the VCP D2 domain ATPase in restoring the distribution of transcripts and proteins and improving various ALS phenotypes, while modulating the VCP interactome. This expands upon previous observations, demonstrating the protective effects of VCP inhibition in ALS iPSMNs.[52,53] VCP inhibitors have shown promise in cancer treatment and have been approved by the FDA. Additionally, numerous studies have reported the rescue of *VCP* mutant disease phenotypes in various *in vitro* and *in vivo* models.[52–54] Nonetheless, further studies are needed to elucidate the precise pathways through which VCP inhibition restores mRNA and protein localization in motor neurons across different ALS genetic backgrounds.

A limitation of our study is that we employed an *in vitro* cellular model, iPSMNs, which may not fully represent the complex environment and characteristics of degenerating motor neurons in ALS. Although iPSMNs provide a disease-relevant cell type, there are inherent differences between *in vitro* cultures and *in vivo* tissues. To address this limitation, we attempted to compare redistributed transcripts in iPSMNs with differentially expressed transcripts in postmortem tissue. However, this comparison is limited because bulk RNA sequencing of spinal cord tissue comprises a mixture of various cell types and is not motor neuron specific. Additionally, the postmortem samples were not subjected to fractionation, which limits our ability to determine the nucleocytoplasmic transcript distributions. Isolating motor neurons from postmortem tissue is technically challenging, particularly for long fragile motor neurons. Although single-nuclear sequencing of ALS postmortem spinal cord can provide insights, it is unable to compare nuclear-to-cytoplasmic ratios.[79] Spatial transcriptomics and spatial proteomics hold promise in elucidating subcellular localization of transcripts and proteins, but their current resolution is insufficient to fully resolve the subcellular landscape of motor neurons.[80,81] Future research should aim to validate these findings in different ALS genetic backgrounds and models. Despite these limitations, our study provides valuable mechanistic insights into the pathogenesis of ALS and highlights a potential therapeutic avenue.

STAR★METHODS

Detailed methods are provided in the online version of this paper and include the following:

- KEY RESOURCES TABLE
- RESOURCE AVAILABILITY
  - Lead contact
  - Materials availability
  - Data and code availability
- EXPERIMENTAL MODEL AND STUDY PARTICIPANT DETAILS
  - Human iPSC-derived motor neuron lines
  - Postmortem tissue
- METHOD DETAILS
  - iPSMN fractionation
  - RNA sequencing
  - Proteomics
  - Western blotting
  - Immunocytochemistry staining and imaging
  - Fluorescent *in situ* hybridization (FISH) and immunofluorescence
  - VCP inhibitor treatment
  - VCP co-immunoprecipitation
  - iPSMN viability, lysosome, oxidative stress, and DNA damage assays
- QUANTIFICATION AND STATISTICAL ANALYSIS
  - Transcriptome analysis
  - RNA-protein interactions
  - Alternative splicing
  - Proteome analysis

SUPPLEMENTAL INFORMATION

Supplemental information can be found online at https://doi.org/10.1016/j.neuron.2023.06.019.

ACKNOWLEDGMENTS

This work was funded by the Francis Crick Institute, which receives its core funding from Cancer Research UK (FC010110), the UK Medical Research Council (FC010110), and the Wellcome Trust (FC010110). O.J.Z. holds a Crick Clinical PhD Fellowship supported by the University College London Hospitals Biomedical Research Centre (BRC689/ED/CB/100130). R.P. holds an MRC Senior Clinical Fellowship (MR/S006591/1) and a Lister Research Prize Fellowship.

We are grateful for advice from members of the Patani laboratory and Drs. Harshil Patel, Konstantin Krismer, Benjamin Lang, and Mathew Talliaferro. The authors thank colleagues at the Francis Crick Institute, particularly for their assistance with RNA sequencing, mass spectrometry, and bioinformatics.

AUTHOR CONTRIBUTIONS

Conceptualization, O.J.Z. and R.P.; software, O.J.Z., A.M.C., and G.K.; formal analysis, O.J.Z., A.M.C., and G.K.; methodology, J.H., Y.W, J.N, G.T., F.I., and M.S.; validation, J.H., Y.W, J.N, G.T., F.I., and M.S.; investigation, O.J.Z., J.H., Y.W, J.N, G.T., F.I., M.S., G.K., and R.P.; data curation, O.J.Z., J.H., Y.W, J.N, G.T., A.M.C., and G.K.; visualization, O.J.Z., A.M.C., and G.K.; resources, R.P.; funding acquisition, R.P.; supervision, G.K. and R.P.; project administration, O.J.Z., G.K., and R.P.; writing – original draft, O.J.Z.; writing – review & editing, O.J.Z., J.H., Y.W, J.N, G.T., F.I., M.S., A.M.C., G.K., and R.P.

DECLARATION OF INTERESTS

R.P. and J.H. are named inventors on a patent related to VCP inhibitors (WO2023281030A3).

Received: October 19, 2022
Revised: May 9, 2023
Accepted: June 22, 2023
Published: July 21, 2023

REFERENCES

1. Taylor, J.P., Brown, R.H., Jr., and Cleveland, D.W. (2016). Decoding ALS: from genes to mechanism. Nature *539*, 197–206.

2. Feldman, E.L., Goutman, S.A., Petri, S., Mazzini, L., Savelieff, M.G., Shaw, P.J., and Sobue, G. (2022). Amyotrophic lateral sclerosis. Lancet *400*, 1363–1380. https://doi.org/10.1016/S0140-6736(22)01272-7.

3. Tyzack, G.E., Luisier, R., Taha, D.M., Neeves, J., Modic, M., Mitchell, J.S., Meyer, I., Greensmith, L., Newcombe, J., Ule, J., et al. (2019). Widespread FUS mislocalization is a molecular hallmark of amyotrophic lateral sclerosis. Brain *142*, 2572–2580.

4. Luisier, R., Tyzack, G.E., Hall, C.E., Mitchell, J.S., Devine, H., Taha, D.M., Malik, B., Meyer, I., Greensmith, L., Newcombe, J., et al. (2018). Intron retention and nuclear loss of SFPQ are molecular hallmarks of ALS. Nat. Commun. *9*, 2010.

5. Diaz-Garcia, S., Ko, V.I., Vazquez-Sanchez, S., Chia, R., Arogundade, O.A., Rodriguez, M.J., Traynor, B.J., Cleveland, D., and Ravits, J. (2021). Nuclear depletion of RNA-binding protein ELAVL3 (HuC) in sporadic and familial amyotrophic lateral sclerosis. Acta Neuropathol. *142*, 985–1001.

6. Bampton, A., Gatt, A., Humphrey, J., Cappelli, S., Bhattacharya, D., Foti, S., Brown, A.-L., Asi, Y., Low, Y.H., Foiani, M., et al. (2021). HnRNP K mislocalisation is a novel protein pathology of frontotemporal lobar degeneration and ageing and leads to cryptic splicing. Acta Neuropathol. *142*, 609–627.

7. Bampton, A., Gittings, L.M., Fratta, P., Lashley, T., and Gatt, A. (2020). The role of hnRNPs in frontotemporal dementia and amyotrophic lateral sclerosis. Acta Neuropathol. *140*, 599–623.

8. Liu, Y.-J., Kuo, H.-C., and Chern, Y. (2021). A system-wide mislocalization of RNA-binding proteins in motor neurons is a new feature of ALS. Neurobiol. Dis. *160*, 105531.

9. Neumann, M., Sampathu, D.M., Kwong, L.K., Truax, A.C., Micsenyi, M.C., Chou, T.T., Bruce, J., Schuck, T., Grossman, M., Clark, C.M., et al. (2006). Ubiquitinated TDP-43 in frontotemporal lobar degeneration and amyotrophic lateral sclerosis. Science *314*, 130–133.

10. Fallini, C., Khalil, B., Smith, C.L., and Rossoll, W. (2020). Traffic jam at the nuclear pore: All roads lead to nucleocytoplasmic transport defects in ALS/FTD. Neurobiol. Dis. *140*, 104835.

11. Kim, H.J., and Taylor, J.P. (2017). Lost in Transportation: Nucleocytoplasmic Transport Defects in ALS and Other Neurodegenerative Diseases. Neuron *96*, 285–297.

12. Chou, C.-C., Zhang, Y., Umoh, M.E., Vaughan, S.W., Lorenzini, I., Liu, F., Sayegh, M., Donlin-Asp, P.G., Chen, Y.H., Duong, D.M., et al. (2018). TDP-43 pathology disrupts nuclear pore complexes and nucleocytoplasmic transport in ALS/FTD. Nat. Neurosci. *21*, 228–239.

13. Zhang, K., Donnelly, C.J., Haeusler, A.R., Grima, J.C., Machamer, J.B., Steinwald, P., Daley, E.L., Miller, S.J., Cunningham, K.M., Vidensky, S., et al. (2015). The C9orf72 repeat expansion disrupts nucleocytoplasmic transport. Nature *525*, 56–61.

14. Woerner, A.C., Frottin, F., Hornburg, D., Feng, L.R., Meissner, F., Patra, M., Tatzelt, J., Mann, M., Winklhofer, K.F., Hartl, F.U., and Hipp, M.S. (2016). Cytoplasmic protein aggregates interfere with nucleocytoplasmic transport of protein and RNA. Science *351*, 173–176.

15. Coyne, A.N., Baskerville, V., Zaepfel, B.L., Dickson, D.W., Rigo, F., Bennett, F., Lusk, C.P., and Rothstein, J.D. (2021). Nuclear accumulation of CHMP7 initiates nuclear pore complex injury and subsequent TDP-43 dysfunction in sporadic and familial ALS. Sci. Transl. Med. *13*, eabe1923. https://doi.org/10.1126/scitranslmed.abe1923.

16. Castelli, L.M., Cutillo, L., Souza, C.D.S., Sanchez-Martinez, A., Granata, I., Lin, Y.-H., Myszczynska, M.A., Heath, P.R., Livesey, M.R., Ning, K., et al. (2021). SRSF1-dependent inhibition of C9ORF72-repeat RNA nuclear export: genome-wide mechanisms for neuroprotection in amyotrophic lateral sclerosis. Mol. Neurodegener. *16*, 53.

17. Kim, J.-E., Hong, Y.H., Kim, J.Y., Jeon, G.S., Jung, J.H., Yoon, B.-N., Son, S.-Y., Lee, K.-W., Kim, J.-I., and Sung, J.-J. (2017). Altered nucleocytoplasmic proteome and transcriptome distributions in an in vitro model of amyotrophic lateral sclerosis. PLoS One *12*, e0176462.

18. Markmiller, S., Sathe, S., Server, K.L., Nguyen, T.B., Fulzele, A., Cody, N., Javaherian, A., Broski, S., Finkbeiner, S., Bennett, E.J., et al. (2021). Persistent mRNA localization defects and cell death in ALS neurons caused by transient cellular stress. Cell Rep. *36*, 109685.

19. Tsai, Y.-L., Mu, Y.C., and Manley, J.L. (2022). Nuclear RNA transcript levels modulate nucleocytoplasmic distribution of ALS/FTD-associated protein FUS. Sci. Rep. *12*, 8180.

20. Corley, M., Burns, M.C., and Yeo, G.W. (2020). How RNA-Binding Proteins Interact with RNA: Molecules and Mechanisms. Mol. Cell *78*, 9–29.

21. Van Nostrand, E.L., Freese, P., Pratt, G.A., Wang, X., Wei, X., Xiao, R., Blue, S.M., Chen, J.-Y., Cody, N.A.L., Dominguez, D., et al. (2020). A large-scale binding and functional map of human RNA-binding proteins. Nature *583*, 711–719.

22. Lin, Y., Liu, T., Cui, T., Wang, Z., Zhang, Y., Tan, P., Huang, Y., Yu, J., and Wang, D. (2020). RNAInter in 2020: RNA interactome repository with increased coverage and annotation. Nucleic Acids Res. *48*, D189–D197.

23. Mauger, O., Lemoine, F., and Scheiffele, P. (2016). Targeted Intron Retention and Excision for Rapid Gene Regulation in Response to Neuronal Activity. Neuron *92*, 1266–1278.

24. Fredericks, A.M., Cygan, K.J., Brown, B.A., and Fairbrother, W.G. (2015). RNA-Binding Proteins: Splicing Factors and Disease. Biomolecules *5*, 893–909.

25. Reed, R., and Cheng, H. (2005). TREX, SR proteins and export of mRNA. Curr. Opin. Cell Biol. *17*, 269–273.

26. Müller-McNicoll, M., Botti, V., de Jesus Domingues, A.M., Brandl, H., Schwich, O.D., Steiner, M.C., Curk, T., Poser, I., Zarnack, K., and Neugebauer, K.M. (2016). SR proteins are NXF1 adaptors that link alternative RNA processing to mRNA export. Genes Dev. *30*, 553–566.

27. Palazzo, A.F., and Lee, E.S. (2018). Sequence Determinants for Nuclear Retention and Cytoplasmic Export of mRNAs and lncRNAs. Front. Genet. *9*, 440.

28. Ho, R., Workman, M.J., Mathkar, P., Wu, K., Kim, K.J., O'Rourke, J.G., Kellogg, M., Montel, V., Banuelos, M.G., Arogundade, O.A., et al. (2021). Cross-Comparison of Human iPSC Motor Neuron Models of Familial and Sporadic ALS Reveals Early and Convergent Transcriptomic Disease Signatures. Cell Syst. *12*, 159–175.e9.

29. Hall, C.E., Yao, Z., Choi, M., Tyzack, G.E., Serio, A., Luisier, R., Harley, J., Preza, E., Arber, C., Crisp, S.J., et al. (2017). Progressive Motor Neuron Pathology and the Role of Astrocytes in a Human Stem Cell Model of VCP-Related ALS. Cell Rep. *19*, 1739–1749.

30. Barthelson, R.A., Lambert, G.M., Vanier, C., Lynch, R.M., and Galbraith, D.W. (2007). Comparison of the contributions of the nuclear and cytoplasmic compartments to global gene expression in human cells. BMC Genom. *8*, 340–415.

31. Benoit Bouvrette, L.P., Cody, N.A.L., Bergalet, J., Lefebvre, F.A., Diot, C., Wang, X., Blanchette, M., and Lécuyer, E. (2018). CeFra-seq reveals broad asymmetric mRNA and noncoding RNA distribution profiles in Drosophila and human cells. RNA *24*, 98–113.

32. Ziff, O.J., Neeves, J., Mitchell, J., Tyzack, G., Martinez-Ruiz, C., Luisier, R., Chakrabarti, A.M., McGranahan, N., Litchfield, K., Boulton, S.J., et al. (2023). Integrated transcriptome landscape of ALS identifies genome instability linked to TDP-43 pathology. Nat. Commun. *14*, 2176.

33. Smethurst, P., Risse, E., Tyzack, G.E., Mitchell, J.S., Taha, D.M., Chen, Y.-R., Newcombe, J., Collinge, J., Sidle, K., and Patani, R. (2020). Distinct responses of neurons and astrocytes to TDP-43 proteinopathy in amyotrophic lateral sclerosis. Brain *143*, 430–440.

34. Tyzack, G.E., Neeves, J., Crerar, H., Klein, P., Ziff, O., Taha, D.M., Luisier, R., Luscombe, N.M., and Patani, R. (2021). Aberrant cytoplasmic intron retention is a blueprint for RNA binding protein mislocalization in amyotrophic lateral sclerosis. Brain *144*, 1985–1993. https://doi.org/10.1093/brain/awab078.

35. Price, A.J., Hwang, T., Tao, R., Burke, E.E., Rajpurohit, A., Shin, J.H., Hyde, T.M., Kleinman, J.E., Jaffe, A.E., and Weinberger, D.R. (2020).

Characterizing the nuclear and cytoplasmic transcriptomes in developing and mature human cortex uncovers new insight into psychiatric disease gene regulation. Genome Res. *30*, 1–11.

36. Humphrey, J., Venkatesh, S., Hasan, R., Herb, J.T., de Paiva Lopes, K., Küçükali, F., Byrska-Bishop, M., Evani, U.S., Narzisi, G., Fagegaltier, D., et al. (2023). Integrative transcriptomic analysis of the amyotrophic lateral sclerosis spinal cord implicates glial activation and suggests new risk genes. Nat. Neurosci. *26*, 150–162. https://doi.org/10.1038/s41593-022-01205-3.

37. Ziff, O.J., Neeves, J., Mitchell, J., Tyzack, G., Ruiz, C.M., McGranahan, N., Luisier, R., Chakrabarti, A.M., Boulton, S.J., Kelly, G., et al. (2022). Meta-analysis of the amyotrophic lateral sclerosis spectrum uncovers genome instability. bioRxiv. https://doi.org/10.1101/2022.08.11.22278516.

38. Courel, M., Clément, Y., Bossevain, C., Foretek, D., Vidal Cruchez, O., Yi, Z., Bénard, M., Benassy, M.-N., Kress, M., Vindry, C., et al. (2019). GC content shapes mRNA storage and decay in human cells. Elife *8*, e49708. https://doi.org/10.7554/eLife.49708.

39. Hamilton, R.S., and Davis, I. (2011). Identifying and searching for conserved RNA localisation signals. Methods Mol. Biol. *714*, 447–466.

40. Lang, B., Armaos, A., and Tartaglia, G.G. (2019). RNAct: Protein-RNA interaction predictions for model organisms with supporting experimental data. Nucleic Acids Res. *47*, D601–D606.

41. Ray, D., Kazan, H., Cook, K.B., Weirauch, M.T., Najafabadi, H.S., Li, X., Gueroussov, S., Albu, M., Zheng, H., Yang, A., et al. (2013). A compendium of RNA-binding motifs for decoding gene regulation. Nature *499*, 172–177.

42. Cook, K.B., Kazan, H., Zuberi, K., Morris, Q., and Hughes, T.R. (2011). RBPDB: a database of RNA-binding specificities. Nucleic Acids Res. *39*, D301–D308.

43. Vaquero-Garcia, J., Barrera, A., Gazzara, M.R., González-Vallinas, J., Lahens, N.F., Hogenesch, J.B., Lynch, K.W., and Barash, Y. (2016). A new view of transcriptome complexity and regulation through the lens of local splicing variations. Elife *5*, e11752.

44. Zhang, X., Smits, A.H., van Tilburg, G.B., Ovaa, H., Huber, W., and Vermeulen, M. (2018). Proteome-wide identification of ubiquitin interactions using UbIA-MS. Nat. Protoc. *13*, 530–550.

45. Koussounadis, A., Langdon, S.P., Um, I.H., Harrison, D.J., and Smith, V.A. (2015). Relationship between differentially expressed mRNA and mRNA-protein correlations in a xenograft model system. Sci. Rep. *5*, 10775.

46. Manno, A., Noguchi, M., Fukushi, J., Motohashi, Y., and Kakizuka, A. (2010). Enhanced ATPase activities as a primary defect of mutant valosin-containing proteins that cause inclusion body myopathy associated with Paget disease of bone and frontotemporal dementia. Gene Cell. *15*, 911–922.

47. Chang, Y.-C., Hung, W.-T., Chang, Y.-C., Chang, H.C., Wu, C.-L., Chiang, A.-S., Jackson, G.R., and Sang, T.-K. (2011). Pathogenic VCP/TER94 alleles are dominant actives and contribute to neurodegeneration by altering cellular ATP level in a Drosophila IBMPFD model. PLoS Genet. *7*, e1001288.

48. Bartolome, F., Wu, H.-C., Burchell, V.S., Preza, E., Wray, S., Mahoney, C.J., Fox, N.C., Calvo, A., Canosa, A., Moglia, C., et al. (2013). Pathogenic VCP mutations induce mitochondrial uncoupling and reduced ATP levels. Neuron *78*, 57–64.

49. Blythe, E.E., Olson, K.C., Chau, V., and Deshaies, R.J. (2017). Ubiquitin- and ATP-dependent unfoldase activity of P97/VCP•NPLOC4•UFD1L is enhanced by a mutation that causes multisystem proteinopathy. Proc. Natl. Acad. Sci. USA *114*, E4380–E4388.

50. Zhang, X., Gui, L., Zhang, X., Bulfer, S.L., Sanghez, V., Wong, D.E., Lee, Y., Lehmann, L., Lee, J.S., Shih, P.-Y., et al. (2015). Altered cofactor regulation with disease-associated p97/VCP mutations. Proc. Natl. Acad. Sci. USA *112*, E1705–E1714.

51. Fernández-Sáiz, V., and Buchberger, A. (2010). Imbalances in p97 co-factor interactions in human proteinopathy. EMBO Rep. *11*, 479–485.

52. Harley, J., Hagemann, C., Serio, A., and Patani, R. (2021). TDP-43 and FUS mislocalization in VCP mutant motor neurons is reversed by pharmacological inhibition of the VCP D2 ATPase domain. Brain Commun. *3*, fcab166. https://doi.org/10.1093/braincomms/fcab166.

53. Wang, F., Li, S., Wang, T.Y., Lopez, G.A., Antoshechkin, I., and Chou, T.F. (2022). P97/VCP ATPase inhibitors can rescue p97 mutation-linked motor neuron degeneration. Brain Commun. *4*, fcac176.

54. Zhang, T., Mishra, P., Hay, B.A., Chan, D., and Guo, M. (2017). Valosin-containing protein (VCP/p97) inhibitors relieve Mitofusin-dependent mitochondrial defects due to VCP disease mutants. Elife *6*, e17834. https://doi.org/10.7554/eLife.17834.

55. Chou, T.-F., Li, K., Frankowski, K.J., Schoenen, F.J., and Deshaies, R.J. (2013). Structure-activity relationship study reveals ML240 and ML241 as potent and selective inhibitors of p97 ATPase. ChemMedChem *8*, 297–312.

56. Chou, T.-F., Bulfer, S.L., Weihl, C.C., Li, K., Lis, L.G., Walters, M.A., Schoenen, F.J., Lin, H.J., Deshaies, R.J., and Arkin, M.R. (2014). Specific inhibition of p97/VCP ATPase and kinetic analysis demonstrate interaction between D1 and D2 ATPase domains. J. Mol. Biol. *426*, 2886–2899.

57. Zhang, G., Li, S., Wang, F., Jones, A.C., Goldberg, A.F.G., Lin, B., Virgil, S., Stoltz, B.M., Deshaies, R.J., and Chou, T.-F. (2021). A covalent p97/VCP ATPase inhibitor can overcome resistance to CB-5083 and NMS-873 in colorectal cancer cells. Eur. J. Med. Chem. *213*, 113148.

58. Chandra, S., and Lusk, C.P. (2022). Emerging Connections between Nuclear Pore Complex Homeostasis and ALS. Int. J. Mol. Sci. *23*, 1329. https://doi.org/10.3390/ijms23031329.

59. Lin, Y.-C., Kumar, M.S., Ramesh, N., Anderson, E.N., Nguyen, A.T., Kim, B., Cheung, S., McDonough, J.A., Skarnes, W.C., Lopez-Gonzalez, R., et al. (2021). Interactions between ALS-linked FUS and nucleoporins are associated with defects in the nucleocytoplasmic transport pathway. Nat. Neurosci. *24*, 1077–1088. https://doi.org/10.1038/s41593-021-00859-9.

60. Basu, S., Rajendra, K.C., Alagar, S., and Bahadur, R.P. (2022). Impaired nuclear transport induced by juvenile ALS causing P525L mutation in NLS domain of FUS: A molecular mechanistic study. Biochim. Biophys. Acta. Proteins Proteom. *1870*, 140766.

61. Zaghlool, A., Niazi, A., Björklund, Å.K., Westholm, J.O., Ameur, A., and Feuk, L. (2021). Characterization of the nuclear and cytosolic transcriptomes in human brain tissue reveals new insights into the subcellular distribution of RNA transcripts. Sci. Rep. *11*, 4076.

62. Timney, B.L., Raveh, B., Mironska, R., Trivedi, J.M., Kim, S.J., Russel, D., Wente, S.R., Sali, A., and Rout, M.P. (2016). Simple rules for passive diffusion through the nuclear pore complex. J. Cell Biol. *215*, 57–76.

63. Georgomanolis, T., Sofiadis, K., and Papantonis, A. (2016). Cutting a Long Intron Short: Recursive Splicing and Its Implications. Front. Physiol. *7*, 598.

64. Lagier-Tourenne, C., Polymenidou, M., Hutt, K.R., Vu, A.Q., Baughn, M., Huelga, S.C., Clutario, K.M., Ling, S.-C., Liang, T.Y., Mazur, C., et al. (2012). Divergent roles of ALS-linked proteins FUS/TLS and TDP-43 intersect in processing long pre-mRNAs. Nat. Neurosci. *15*, 1488–1497.

65. Matoulkova, E., Michalova, E., Vojtesek, B., and Hrstka, R. (2012). The role of the 3' untranslated region in post-transcriptional regulation of protein expression in mammalian cells. RNA Biol. *9*, 563–576.

66. Ciolli Mattioli, C., Rom, A., Franke, V., Imami, K., Arrey, G., Terne, M., Woehler, A., Akalin, A., Ulitsky, I., and Chekulaeva, M. (2019). Alternative 3' UTRs direct localization of functionally diverse protein isoforms in neuronal compartments. Nucleic Acids Res. *47*, 2560–2573.

67. Berkovits, B.D., and Mayr, C. (2015). Alternative 3' UTRs act as scaffolds to regulate membrane protein localization. Nature *522*, 363–367.

68. Burke, J.M., Ripin, N., Ferretti, M.B., St Clair, L.A., Worden-Sapper, E.R., Sawyer, S.L., Perera, R., Lynch, K.W., and Parker, R. (2022). RNase L-mediated RNA decay alters 3' end formation and splicing of host mRNAs. Preprint at bioRxiv. https://doi.org/10.1101/2022.01.28.478180.

69. Ederle, H., Funk, C., Abou-Ajram, C., Hutten, S., Funk, E.B.E., Kehlenbach, R.H., Bailer, S.M., and Dormann, D. (2018). Nuclear egress

of TDP-43 and FUS occurs independently of Exportin-1/CRM1. Sci. Rep. *8*, 7084.

70. Gaiani, A., Martinelli, I., Bello, L., Querin, G., Puthenparampil, M., Ruggero, S., Toffanin, E., Cagnin, A., Briani, C., Pegoraro, E., and Sorarù, G. (2017). Diagnostic and Prognostic Biomarkers in Amyotrophic Lateral Sclerosis: Neurofilament Light Chain Levels in Definite Subtypes of Disease. JAMA Neurol. *74*, 525–532.
71. Strong, M.J., Volkening, K., Hammond, R., Yang, W., Strong, W., Leystra-Lantz, C., and Shoesmith, C. (2007). TDP43 is a human low molecular weight neurofilament (hNFL) mRNA-binding protein. Mol. Cell. Neurosci. *35*, 320–327.
72. Demy, D.L., Campanari, M.L., Munoz-Ruiz, R., Durham, H.D., Gentil, B.J., and Kabashi, E. (2020). Functional Characterization of Neurofilament Light Splicing and Misbalance in Zebrafish. Cells *9*, 1238. https://doi.org/10.3390/cells9051238.
73. Chen, H., Qian, K., Du, Z., Cao, J., Petersen, A., Liu, H., Blackbourn, L.W., Huang, C.L., Errigo, A., Yin, Y., et al. (2014). Modeling ALS with iPSCs reveals that mutant SOD1 misregulates neurofilament balance in motor neurons. Cell Stem Cell *14*, 796–809.
74. Mejzini, R., Flynn, L.L., Pitout, I.L., Fletcher, S., Wilton, S.D., and Akkari, P.A. (2019). ALS Genetics, Mechanisms, and Therapeutics: Where Are We Now? Front. Neurosci. *13*, 1310.
75. Mann, J.R., Gleixner, A.M., Mauna, J.C., Gomes, E., DeChellis-Marks, M.R., Needham, P.G., Copley, K.E., Hurtle, B., Portz, B., Pyles, N.J., et al. (2019). RNA Binding Antagonizes Neurotoxic Phase Transitions of TDP-43. Neuron *102*, 321–338.e8.
76. Milicevic, K., Rankovic, B., Andjus, P.R., Bataveljic, D., and Milovanovic, D. (2022). Emerging Roles for Phase Separation of RNA-Binding Proteins in Cellular Pathology of ALS. Front. Cell Dev. Biol. *10*, 840256.
77. Gasset-Rosa, F., Lu, S., Yu, H., Chen, C., Melamed, Z., Guo, L., Shorter, J., Da Cruz, S., and Cleveland, D.W. (2019). Cytoplasmic TDP-43 De-mixing Independent of Stress Granules Drives Inhibition of Nuclear Import, Loss of Nuclear TDP-43, and Cell Death. Neuron *102*, 339–357.e7.
78. Buchan, J.R., Kolaitis, R.-M., Taylor, J.P., and Parker, R. (2013). Eukaryotic stress granules are cleared by autophagy and Cdc48/VCP function. Cell *153*, 1461–1474.
79. Blum, J.A., and Gitler, A.D. (2022). Singling out motor neurons in the age of single-cell transcriptomics. Trends Genet. *38*, 904–919.
80. Maniatis, S., Äijö, T., Vickovic, S., Braine, C., Kang, K., Mollbrink, A., Fagegaltier, D., Andrusivová, Ž., Saarenpää, S., Saiz-Castro, G., et al. (2019). Spatiotemporal dynamics of molecular pathology in amyotrophic lateral sclerosis. Science *364*, 89–93.
81. Lundberg, E., and Borner, G.H.H. (2019). Spatial proteomics: a powerful discovery tool for cell biology. Nat. Rev. Mol. Cell Biol. *20*, 285–302.
82. Deneault, E., Chaineau, M., Nicouleau, M., Castellanos Montiel, M.J., Franco Flores, A.K., Haghi, G., Chen, C.X.-Q., Abdian, N., Shlaifer, I., Beitel, L.K., and Durcan, T.M. (2022). A streamlined CRISPR workflow to introduce mutations and generate isogenic iPSCs for modeling amyotrophic lateral sclerosis. Methods *203*, 297–310.
83. Sigurgeirsson, B., Emanuelsson, O., and Lundeberg, J. (2014). Sequencing degraded RNA addressed by 3' tag counting. PLoS One *9*, e91851.
84. Ewels, P.A., Peltzer, A., Fillinger, S., Patel, H., Alneberg, J., Wilm, A., Garcia, M.U., Di Tommaso, P., and Nahnsen, S. (2020). The nf-core framework for community-curated bioinformatics pipelines. Nat. Biotechnol. *38*, 276–278.
85. Ziff, O.J., Taha, D.M., Crerar, H., Clarke, B.E., Chakrabarti, A.M., Kelly, G., Neeves, J., Tyzack, G.E., Luscombe, N.M., and Patani, R. (2021). Reactive astrocytes in ALS display diminished intron retention. Nucleic Acids Res. *49*, 3168–3184.
86. Moggridge, S., Sorensen, P.H., Morin, G.B., and Hughes, C.S. (2018). Extending the Compatibility of the SP3 Paramagnetic Bead Processing Approach for Proteomics. J. Proteome Res. *17*, 1730–1740.
87. Harley, J., and Patani, R. (2020). Stress-Specific Spatiotemporal Responses of RNA-Binding Proteins in Human Stem Cell-Derived Motor Neurons. Int. J. Mol. Sci. *21*, 8346.
88. Love, M.I., Huber, W., and Anders, S. (2014). Moderated estimation of fold change and dispersion for RNA-seq data with DESeq2. Genome Biol. *15*, 550.
89. Ou, J., and Zhu, L.J. (2019). trackViewer: a Bioconductor package for interactive and integrative visualization of multi-omics data. Nat. Methods *16*, 453–454.
90. Attig, J., Agostini, F., Gooding, C., Chakrabarti, A.M., Singh, A., Haberman, N., Zagalak, J.A., Emmett, W., Smith, C.W.J., Luscombe, N.M., and Ule, J. (2018). Heteromeric RNP Assembly at LINEs Controls Lineage-Specific RNA Processing. Cell *174*, 1067–1081.e17.
91. Sloan, C.A., Chan, E.T., Davidson, J.M., Malladi, V.S., Strattan, J.S., Hitz, B.C., Gabdank, I., Narayanan, A.K., Ho, M., Lee, B.T., et al. (2016). ENCODE data at the ENCODE portal. Nucleic Acids Res. *44*, D726–D732.
92. Krismer, K., Bird, M.A., Varmeh, S., Handly, E.D., Gattinger, A., Bernwinkler, T., Anderson, D.A., Heinzel, A., Joughin, B.A., Kong, Y.W., et al. (2020). Transite: A Computational Motif-Based Analysis Platform That Identifies RNA-Binding Proteins Modulating Changes in Gene Expression. Cell Rep. *32*, 108064.
93. Vaquero-Garcia, J., Aicher, J.K., Jewell, P., Gazzara, M.R., Radens, C.M., Jha, A., Green, C.J., Norton, S.S., Lahens, N.F., Grant, G.R., et al. (2021). RNA splicing analysis using heterogeneous and large RNA-seq datasets. Preprint at bioRxiv. https://doi.org/10.1101/2021.11.03.467086.
94. Slaff, B., Radens, C.M., Jewell, P., Jha, A., Lahens, N.F., Grant, G.R., Thomas-Tikhonenko, A., Lynch, K.W., and Barash, Y. (2021). MOCCASIN: a method for correcting for known and unknown confounders in RNA splicing analysis. Nat. Commun. *12*, 3353.
95. Cox, J., and Mann, M. (2008). MaxQuant enables high peptide identification rates, individualized ppb-range mass accuracies and proteome-wide protein quantification. Nat. Biotechnol. *26*, 1367–1372.
96. Hein, M.Y., Hubner, N.C., Poser, I., Cox, J., Nagaraj, N., Toyoda, Y., Gak, I.A., Weisswange, I., Mansfeld, J., Buchholz, F., et al. (2015). A human interactome in three quantitative dimensions organized by stoichiometries and abundances. Cell *163*, 712–723.

Please cite this article in press as: Ziff et al., Nucleocytoplasmic mRNA redistribution accompanies RNA binding protein mislocalization in ALS motor neurons and is restored by VCP ATPase inhibition, Neuron (2023), https://doi.org/10.1016/j.neuron.2023.06.019

STAR★METHODS

KEY RESOURCES TABLE

REAGENT or RESOURCE	SOURCE	IDENTIFIER
Antibodies		
Mouse monoclonal anti-γH2AX	Millipore	Cat#05–636; RRID: AB_309864
Mouse monoclonal anti-SMI-32	BioLegend	Cat#801701; RRID: AB_2564642
Goat polyclonal anti-ChAT	Millipore	Cat#AB144P; RRID: AB_90661
Chicken polyclonal anti-βIII-tubulin	Abcam	Cat#ab41489; RRID: AB_727049
Rabbit polyclonal anti-TDP-43	Proteintech	Cat#12892-1-AP; RRID: AB_2200505
Mouse monoclonal anti-FUS	Santa Cruz	Cat#sc-47711; RRID: AB_2105208
Rabbit polyclonal anti-FUS	Proteintech	Cat#11570-1-AP; RRID: AB_2247082
Rabbit monoclonal anti-Vinculin	ThermoFisher Scientific	Cat#700062; RRID: AB_2532280
Rabbit polyclonal anti-histone3	Abcam	Cat#Ab1791; RRID: AB_302613
Mouse monoclonal anti-VCP	ThermoFisher Scientific	Cat#MA3-004; RRID: AB_2214638
Chemicals, peptides, and recombinant proteins		
Essential 8 Medium media	Life Technologies	Cat#A1517001
Geltrex	Life Technologies	Cat#A1413302
EDTA	Life Technologies	Cat#15575020
Dorsomorphin	Tocris Bioscience	Cat#3093
SB431542	Tocris Bioscience	Cat#1614
CHIR99021	Tocris Bioscience	Cat#4423
Retinoic acid	Sigma Aldrich	Cat# R2625
Puromorphamine	Sigma Aldrich	Cat#540220
Compound E	Biotechne	Cat#6476
RiboLock RNase Inhibitor	Thermo Fisher Scientific	Cat#EO0381
HALT Protease Inhibitor Complex	Thermo Fisher Scientific	Cat#78429
Formamide	Themo Fisher Scientific	Cat#17899
Denatured salmon sperm DNA	Merck	Cat#D7656
Dextran sulfate	Merck	Cat#D6001
UltraPure BSA	Thermo Fisher Scientific	Cat#AM2616
ML240	Sigma Aldrich	Cat#SML1071; CAS: 1346527-98-7
CB-5083	Cayman	Cat#19311; CAS: 1542705-92-9
DBeQ	Aobious	Cat#AOB6826; CAS: 177355-84-9
NMS-873	Aobious	Cat#AOB4921; CAS: 1418013-75-8
Critical commercial assays		
Ambion PARIS nucleocytoplasmic fractionation kit	ThermoFisher Scientific	Cat#AM1921
QIAshredder	Qiagen	Cat#79656
NEBNext Ultra II Directional RNA Library kit for Illumina	New England BioLabs	Cat#E7760L
ViewRNA Cell Plus Assay Kit	Thermo Fisher Scientific	Cat#88-19000-99
Sytox™ Green Nucleic Acid Stain	Invitrogen	Cat#S7020
LysoTracker™ Deep Red	Invitrogen	Cat#L12492
Hoechst 33342	Invitrogen	Cat#H3570
CellROX™ Green Reagent	Invitrogen	Cat#C10444
DL-dithiothreitol	Sigma Aldrich	Cat#D5545
Iodoacetamide	Sigma Life Science	Cat#I1149
Pierce Trypsin Protease MS-grade	ThermoFisher Scientific	Cat#90057
Ammonium bicarbonate	Honeywell	Cat#40867

(*Continued on next page*)

Continued

REAGENT or RESOURCE	SOURCE	IDENTIFIER
Deposited data		
RNA sequencing data	This paper	GEO: GSE214017
Mass Spectrometry	This paper	ProteomeXchange: PXD037107
Existing postmortem RNA sequencing data	New York Genome Center and Target ALS	GEO: GSE137810
Existing CLIP data	https://www.encodeproject.org/	N/A
Experimental models: Cell lines		
Human: CTRL1 iPSC line	Hall et al.[29] (in house)	N/A
Human: CTRL2 iPSC line	Coriell	ND41866*C
Human: CTRL3 iPSC line	ThermoFisher Scientific	A18945
Human: CTRL4 iPSC line	Hall et al.[29] (in house)	N/A
Human: CTRL5 iPSC line	Cedars Sinai	CS02iCTR-NTn4
Human: CTRL6 iPSC line	NIH CRM	CRMi003-A
Human: VCP1 R155C iPSC line	Hall et al.[29] (in house)	N/A
Human: VCP2 R155C iPSC line	Hall et al.[29] (in house)	N/A
Human: VCP3 R191Q iPSC line	Hall et al.[29] (in house)	N/A
Human: VCP4 R191Q iPSC line	Hall et al.[29] (in house)	N/A
Human: VCP5 R191Q knock in iPSC line	Synthego	CRMi003-A - edited by Synthego
Human: VCP6 R191Q knock in iPSC line	Synthego	CRMi003-A - edited by Synthego
Human: TDP-43 n1 G298S iPSC line	Cedars Sinai	CS47iALS-TDPnxx
Human: TDP-43 n2 G298S iPSC line	Cedars Sinai	TALSTDP-47.10
Oligonucleotides		
5′-Cy3- oligo-d(T) probes	Genelink	Cat#26-4322-02
NEFL RNA-FISH probes	ThermoFisher Scientific	Cat#VA1-3003598-VCP
Software and algorithms		
R project for Statistical Computing v4.2.0	CRAN	RRID: SCR_001905
Tidyverse	CRAN	RRID: SCR_019186
DESeq2	Bioconductor	RRID: SCR_015687
nfcore/rnaseq pipeline v3.9	nf-co.re/rnaseq	N/A
TrimGalore!	Babraham	RRID: SCR_011847
SortMeRNA	Bioinfo	RRID: SCR_014402
STAR v2.6.1	RNA-STAR	RRID: SCR_004463
Salmon	https://combine-lab.github.io/salmon/	RRID: SCR_017036
tximport	https://github.com/mikelove/tximport	RRID: SCR_016752
FastQC	Babraham	RRID: SCR_014583
RSeQC	https://rseqc.sourceforge.net/	RRID: SCR_005275
Qualimap	http://qualimap.bioinfo.cipf.es/	RRID: SCR_001209
dupRadar	Bioconductor	N/A
Preseq	http://smithlabresearch.org/software/preseq/	RRID: SCR_018664
MultiQC	http://multiqc.info/	RRID: SCR_014982
trackViewer	Bioconductor	N/A
ComplexHeatmap	Bioconductor	RRID: SCR_017270
g:Profiler2	Bioconductor	N/A
GenomicScores	Bioconductor	N/A
RNAct	rnact.crg.eu	N/A
Transite	Transite.mit.edu	N/A
GenomicRanges	Bioconductor	RRID: SCR_000025
MAJIQ v2.4	https://majiq.biociphers.org/	RRID: SCR_016706

(*Continued on next page*)

Continued

REAGENT or RESOURCE	SOURCE	IDENTIFIER
MaxQuant v2.0.3.1	http://www.biochem.mpg.de/5111795/maxquant	RRID: SCR_014485
DEP v1.11.0	Bioconductor	RRID: SCR_023090
Limma	Bioconductor	RRID: SCR_010943
Harmony High-Content Imaging and Analysis Software 5.0	PerkinElmer	https://www.perkinelmer.com/uk/product/harmony-5-1-office-hh17000012
ImageJ v1.53	National Institutes of Health, USA	https://imagej.nih.gov/ij/
CellProfiler	Broad Institute	https://cellprofiler.org
Other		
Code resource website for this publication	This paper	https://github.com/ojziff/als_mrna_rbp_localisation

RESOURCE AVAILABILITY

Lead contact

Further information and requests for resources should be directed to the lead contact, Rickie Patani (rickie.patani@ucl.ac.uk).

Materials availability

This study did not generate new unique reagents.

Data and code availability

RNA sequencing data have been deposited at GEO and are publicly available as of the date of publication under accession number GEO: GSE214017. This paper analyses existing postmortem RNA sequencing data under accession GEO: GSE137810. Mass Spectrometry data have been deposited in the ProteomeXchange Consortium via the PRIDE partner repository under identifier ProteomeXchange: PXD037107. All original code has been deposited at GitHub and is publicly available as of the date of publication at https://github.com/ojziff/als_mrna_rbp_localisation.

EXPERIMENTAL MODEL AND STUDY PARTICIPANT DETAILS

Human iPSC-derived motor neuron lines

iPSC lines were derived from skin biopsies of healthy donors or ALS patients harboring *VCP* or *TARDBP* mutations. Informed consent was obtained from all subjects. Experimental protocols were all carried out according to approved regulations and guidelines by UCL Hospitals National Hospital for Neurology and Neurosurgery and UCL Institute of Neurology joint research ethics committee (09/0272). iPSC lines were used from four controls (CTRL1, 78 y.o male; CTRL3, fetal female; CTRL4 51 y.o female; CTRL6 fetal male), two ALS patients with *VCP* mutations (two clones VCP1 and VCP2 were from a 43 y.o female patient with a *VCP* R155C mutation; two clones VCP3 and VCP4 were from a 36 y.o male patient with a VCP R191Q mutation), and two ALS patients with *TARDBP* G298S mutations (64 y.o male, and 68 y.o male). Insertion of the R191Q mutation in VCP was introduced into two clones of CTRL6 by Synthego using CRISPR gene editing[82] (Table S1A).

iPSCs were maintained with Essential 8 Medium media (Life Technologies) on Geltrex (Life Technologies) at 37°C and 5% carbon dioxide. iPSCs were passaged when reaching 70% confluency using EDTA (Life Technologies, 0.5 mM). iPSC lines used can be found in Table S1. iPSC cultures underwent differentiation into spinal cord motor neurons as previously described.[29] Briefly, iPSCs were plated to 100% confluency and then differentiated to a spinal neural precursor fate by sequential treatment with small molecules, 0–7: 1 μM Dorsomorphin (Tocris Bioscience), 2 μM SB431542 (Tocris Bioscience), and 3.3 μM CHIR99021 (Tocris Bioscience), day 7–14: 0.5 μM retinoic acid (Sigma Aldrich) and 1 μM Purmorphamine (Sigma Aldrich), day 14–18: 0.1 μM Purmorphamine. After neural conversion and patterning, 0.1 μM Compound E (Bio-techne) was added to promote terminal differentiation into spinal cord motor neurons.

Postmortem tissue

Postmortem spinal cord ALS RNA-sequencing samples were acquired from publicly available data (GEO: GSE137810) from the New York Genome Center (NYGC) ALS and Target ALS consortia. Samples from non-spinal cord sites were excluded. In cases where multiple spinal cord samples were available from an individual donor, only the cervical cord sample was included. A total of 271 spinal cord samples were analyzed, including 57 healthy donors and 214 ALS patients. The ALS patient samples consisted of various mutations (*C9orf72, SOD1, FUS* and 8 other pathogenic mutations) but most were from patients without an identifiable pathogenic

mutation.[32] Ribosomal depletion was used for RNA extraction due to the high levels of RNA degradation in postmortem tissue.[36,83] Raw reads were downloaded and processed using the nf-core fetchngs and rnaseq pipelines respectively.[84]

METHOD DETAILS

iPSMN fractionation

iPSMNs underwent subcellular fractionation into nuclear and cytoplasmic compartments as previously described.[34,85] This was achieved using the Ambion PARIS kit (Thermo Fisher Scientific) cell fractionation buffer, following the manufacturer's protocol using an 8M urea nuclear lysis buffer containing 50 mM Tris-HCL (pH8), 100 mM NaCl, 0.1% SDS, and 1 mM dithiothreitol (DTT). The cytosolic fraction was obtained by lysing iPSMNs directly in an ice-cold cell fractionation buffer. Lysates were centrifuged for 3 min at 500 x g at 4°C. The supernatant was further centrifuged at maximum speed in a bench centrifuge at 4°C for 1 min, and the resulting supernatant was then processed as the cytosolic fraction. Nuclear pellets from the first centrifugation step were gently washed once with cell fractionation buffer and then lysed on ice for 30 min in an 8 M Urea Nuclear Lysis Buffer. The resulting nuclear fraction was then homogenized using a QIAshredder (Qiagen) to shred chromatin and reduce viscosity. Both lysis buffers were supplemented with 0.1 U/μl RiboLock RNase Inhibitor (Thermo Fisher Scientific) and HALT Protease Inhibitor Complex (Thermo Fisher Scientific).

RNA sequencing

Poly(A)+ selected reverse-stranded RNA sequencing libraries were prepared from nuclear and cytoplasmic fractions using the NEBNext Ultra II Directional RNA Library kit for Illumina, with 500 ng of total RNA as input. Libraries were sequenced on the NovoSeq 6000 platform. A mean of 189 (range 143–368) million 100 bp paired-end strand-specific reads were sequenced per sample. mRNA sequencing reads were processed using the nf-core/rna-seq v3.9 pipeline.[84] Raw reads underwent adaptor trimming with Trim Galore, removal of ribosomal RNA with SortMeRNA, alignment to Ensembl GRCh38.99 human reference genome using splice-aware aligner, STAR v2.6.1 and BAM level quantification with Salmon to enable transcript level counting. Detailed quality control of raw and aligned reads were assessed by utilizing FastQC, RSeQC, Qualimap, dupRadar, Preseq and MultiQC tools. All libraries generated in this study had <0.1% rRNA, <1% mtDNA, <0.4% mismatch error, and >90% strandedness (Table S1B).

Proteomics

Samples from the nucleus and cytoplasm were prepared for mass spectrometry using an SP3 (Single Photon Counting) protocol.[86] Samples were reduced by the addition of DTT to a final concentration of 10 mM, incubated at RT for 20 min, then alkylated with iodoacetamide to a final concentration of 10 mM, and then incubated at RT for a further 30 min in the dark. Sera_Mag beads were used to remove contaminating reagents, such as detergent and salts. A 1:1 mixture of carboxylated magnetic beads and HILIC paramagnetic beads was added to the protein samples. Ethanol was added to a specific final concentration (100% v/v) to induce protein binding. The mixture was incubated in a thermomixer at 24°C for 5 min at 1000 rpm. Following this, the bead mixture was washed four times with 80% ethanol before resuspending the beads in 50 μL of 100 mM ammonium hydrogen carbonate containing 0.8 μg of trypsin. The bead mixture was then sonicated briefly in a bath sonicator to fully disaggregate the beads, and the digestion was performed for 18 h at 37°C in a thermomixer. Following digestion, the beads were centrifuged at 20,000 x g at 24°C for 1 min. The supernatants were removed and collected into clean tubes. Recovered peptides were acidified by the addition of formic acid to a 1% v/v final concentration.

The resulting peptides were analyzed by nano-scale capillary LC-MS/MS using an Ultimate U3000 HPLC (ThermoScientific Dionex, San Jose, USA) to deliver a flow of approximately 300 nL/min. A C18 Acclaim PepMap100 5 μm, 75 μm × 20 mm nanoViper (ThermoScientific Dionex, San Jose, USA), trapped the peptides prior to separation on an EASY-Spray PepMap RSLC 2 μm, 100 Å, 75 μm × 500 mm nanoViper column. Peptides were eluted with a 90 min gradient of acetonitrile (2% v/v to 80% v/v). The analytical column outlet was directly interfaced, via a nano-flow electrospray ionization source, to a hybrid quadrupole orbitrap mass spectrometer (Lumos Tribrid Orbitrap mass spectrometer, ThermoScientific, San Jose, USA). Data dependent analysis (DDA) was carried out, using a resolution of 120,000 for the full MS spectrum, followed by MS/MS spectra acquisition in the linear ion trap using "TopS" mode. MS spectra were collected over an m/z range of 300–1800. MS/MS scans were collected using a threshold energy of 32% for collision-induced dissociation.

Western blotting

Protein lysates were loaded onto NuPAGE, 4–12%, Bis-Tris protein gels (Invitrogen) and subjected to electrophoresis before being transferred onto nitrocellulose membranes (Biorad). Blocking was performed in PBS, 0.1% tween, and 5% bovine serum albumin for 1 h at room temperature and incubated overnight with rabbit anti-vinculin (1:1000, ThermoFisher 42H89L44) and rabbit anti-histone 3 (1:1000, Abcam ab1791). Following washes, membranes were incubated for 1 h at room temperature with fluorescent secondary anti-rabbit antibody (1:10000, LI-COR IRDye). Membranes were imaged using Odyssey Fc Imaging System (LI-COR).

Immunocytochemistry staining and imaging

Motor neurons at day 24 of differentiation were fixed in 4% paraformaldehyde solutions (PFA) in PBS for 10 min at room temperature. Cells were permeabilized and non-specific antibody blocked in 0.3% Triton X containing 5% bovine serum albumin (BSA) (Sigma) in PBS for 1 h. Primary antibodies SMI-32 (BioLegend; 801701; mouse; 1:1000), ChAT (Millipore; AB144P; goat; 1:100), βIII-tubulin (Abcam; ab41489; chicken; 1:1000), TDP-43 (Proteintech; 12892-1-AP; rabbit; 1:500), FUS (Santa Cruz; sc-47711; mouse; 1:200), FUS (Proteintech; 11570-1-AP; rabbit; 1:500) were made up in 5% BSA and incubated overnight at 4°C. Following 2 washes with PBS, cells were incubated with a species-specific Alexa Fluor-conjugated secondary antibody (Life Technologies, 1:1000) in 5% BSA for 90 min at room temperature in the dark. Cells were washed once in PBS containing DAPI, 4′,6-diamidino-2-phenylindole nuclear stain (1:1000) for 10 min. Cells were imaged immediately or left in PBS at 4°C. Image acquisition was done using the Opera Phenix High-Content Screening System (PerkinElmer). Images were acquired with a 40× objective as confocal z-stacks with a z-step of 1 μm, which were processed to obtain a maximum intensity projection.

Fluorescent *in situ* hybridization (FISH) and immunofluorescence

iPSC-derived motor neurons were grown on Polyethyleneimine (Sigma) and Geltrex-coated sterile 8-well μ-Slides (Ibidi) then washed in 1x PBS and fixed for RNA fluorescent *in situ* hybridization (FISH) experiments. For targeted NEFL RNA-FISH, motor neurons were fixed and stained using ViewRNA Cell Plus Assay Kit (Thermo Fisher Scientific). Antibody staining, probe hybridization and amplification were carried out in accordance with manufacturer guidelines. Immunolabelling was performed with βIII-Tubulin primary antibody (Abcam, ab41489), followed by species-specific 488 Alexa-Fluor conjugated secondary antibody (1:1000) each for 1 h at room temperature. NEFL probes (Thermo Fisher Scientific, VA1-3003598-VCP) were hybridized for 2h at 40°C, and pre-amplifier, amplifier, and fluorescent label probes each for 1h at 40°C. DAPI counterstain was applied for 10 min at room temperature and then cells were maintained in 1x PBS supplemented with RNase inhibitor. Cells were imaged using an 880 Laser Scanning Confocal Microscope (Zeiss), with 63x/40x, 1.4 N.A. oil immersion objective; the pinhole was set to a diameter of 1 Airy unit. Images were obtained as z-stacks with a z-plane step of 1 μm, from a minimum of 5 fields per biological replicate. Images were processed and arranged to obtain a maximum intensity projection using Fiji/ImageJ. Image masking, filtering and output measurements were performed with CellProfiler pipelines. NEFL RNA-FISH absolute counts were generated from nuclear and cytoplasmic masks.

VCP inhibitor treatment

Four VCP inhibitors were used in this study, namely ML240 (Sigma Aldrich; SML1071; CAS: 1346527-98-7), CB-5083 (Cayman; 19311; CAS: 1542705-92-9), DBeQ (Aobious; AOB6826; CAS: 177355-84-9), and NMS-873 (Aobious; AOB4921; CAS: 1418013-75-8). VCP inhibitor treatment was performed on day 24 of motor neuron differentiation, the medium was changed to fresh medium containing either: 1 μM of ML240 for 2 h, 1 μM of CB-5083 for 3 h, 5 μM of DBeQ for 3 h, 10 μM of NMS-873 for 3 h, or the same volume of DMSO as the untreated control before harvesting.

VCP co-immunoprecipitation

Motor neurons were lysed in 500 μl of lysis buffer containing 50 mM Tris-HCl pH 7.4, 150 mM NaCl, 1% NP40, 2 mM MgCl2, and protease inhibitors on ice. Samples were sonicated with the Bioruptor for 10 cycles with alternating 30 s on/off at low intensity. Protein concentration was measured with the Quick Start Bradford Protein Assay according to manufacturer instructions. Protein A Dynabeads and VCP or IgG antibody complexes were prepared by resuspending 100μL of washed protein A dynabeads with 8μg of antibody for each condition and incubated for 1 h at room temperature. The antibody-bead complexes were then washed 3 times with lysis buffer. Extracts containing 500 μg of protein were incubated with protein A Dynabead only for 3 h at 4°C on a rotator before a 16 h incubation with the bead + antibody complexes at 4°C. The beads were collected and washed 4 times with lysis buffer and 3 times in 50 mM of ammonium bicarbonate. The immunoprecipitated proteins were analyzed by SDS-PAGE and immunoblotting for validation using the VCP antibody (MA3-004, ThermoFisher). VCP interacting proteins were analyzed by mass spectrometry.

Pulldown of iPSMN samples in 50 μL of 50mM NH4HCO3 was prepared using in-solution digest protocol. Samples were reduced with 10 mM DTT for 1 h at 37°C in a thermomixer. Proteins were alkylated with 20 mM iodoacetamide for 30 min in the dark at room temperature. Trypsin 0.4 μg was added and digested overnight at 37°C. Digestion reactions were quenched with 10% formic acid. Clean-up was performed using EV2018 EVOTIP PURE. Desalting was performed according to manufacturer instructions. Tips were conditioned with 0.1% formic acid in acetonitrile, equilibrated with 0.1% formic acid in water and 1 μg of each digested sample was loaded onto Evotips. The liquid was passed through the pipette with a light centrifugation step. Peptides were eluted using 50% acetonitrile and 0.1% TFA buffer. Samples were evaporated in a Speedvac and re-suspended in 30 μL of 0.1% (v/v) formic acid in LCMS-grade water. The recovered peptide samples were analyzed by LC-MS/MS using an Orbitrap Eclipse (Thermo Fisher) coupled to an UltiMate 3000 RSLCnano (Thermo Fisher). Samples were loaded onto a 50 cm, 75 μmPepMap RSLC C18 column (ES903) (Each sample was injected in technical triplicate).

iPSMN viability, lysosome, oxidative stress, and DNA damage assays

Before live cell imaging for the viability assay and lysosomal activity detection, motor neurons were loaded with 500nM Sytox green nucleic acid stain (Invitrogen, S7020) to label dead cells, 50nM LysoTracker deep red dye (Invitrogen, L12492) to track lysosomes, and 5 μg/ml Hoechst (Invitrogen, H3570) to count the total number of cells for 15 min at 37°C. Oxidative stress detection was

conducted using 5 μM CellROX green reagent (Invitrogen, C10444) and Hoechst (Invitrogen, H3570) for 30 min at 37°C. Neurons were then fixed with 4% PFA at room temperature for 10 min before CellROX imaging. For DNA damage assay, motor neurons were first fixed in 4% PFA for 10 min, and then permeabilized and blocked using 0.3% Triton X and 5% BSA for 1 h at room temperature. γH2AX (Millipore; 05–636; mouse; 1:1000) and βIII-tubulin (Abcam; ab41489; chicken; 1:1000) antibodies were made up in 0.15% Triton X and 2.5% BSA and applied overnight at 4°C. Species-specific Alexa Fluor-conjugated secondary antibodies (Life Technologies, 1:1000) were added onto cells for 90 min, followed by counterstaining with DAPI for 10 min at room temperature before imaging.

Images were acquired via the Opera Phenix Plus High-Content Confocal Screening System (PerkinElmer). 9–12 fields of view were taken for each well, with each condition acquired in technical duplication. z stack images with an interval of 1 μm were taken with a 40× objective and processed to maximum intensity projection before being analyzed through the Harmony Imaging and Analysis Software (PerkinElmer). 37°C and 5% CO_2 were applied for Sytox and LysoTracker live cell imaging. Cell density was measured, and wells with nuclei object number ≥800 in all fields were analyzed for lysosomal localization assay. The average intensity and foci number measurements were calculated per cell and then averaged across each well. For the soma measurement, a 1.5 μm cytoplasmic region was defined around the nucleus.[52,87] Lysosomal spots were identified through Harmony Find Spot Method C with radius ≤ 0.86 μm, LysoTracker intensity to region intensity >1.5, and filtered by the intensity of spot maximum ≥500, spot contrast ≥0.2, and corrected spot intensity ≥40. For the oxidative stress assay, wells with ≥800 cells were analyzed. The sum of nuclear CellROX intensity was calculated per cell and averaged across each well. For the DNA damage assay, γH2AX spots were identified in the nuclear region using the Harmony Find Spot Method C with radius ≤1.02 μm, spot contrast >0.26, an uncorrected spot to region intensity >3, and distance ≥0.63 μm, and wells with ≥100 cells were analyzed. 9 fields of view were taken for each well and the mean number of γH2AX spots per nucleus was calculated across the well.

QUANTIFICATION AND STATISTICAL ANALYSIS

Transcriptome analysis

Salmon quantified transcript abundance files were imported to R v4.2.0 using tximport. Transcript counts were normalized and transformed using the variance stabilizing transformation function in DESeq2.[88] These transformed values were utilized in the principal component analysis (PCA) and unsupervized hierarchical clustering. Individual principal components (PCs) were calculated based on the 500 highest variance genes using the plotPCA function, and individual PC transcript loadings were extracted with the prcomp function. Nucleocytoplasmic fractionation quality control was performed by classifying mapped reads as originating from exonic (5′ UTR, CDS, and 3′ UTR), intronic, or intergenic genome regions using Qualimap genomic origin and RSeQC read_distribution.py tools. The human cortex transcriptome database of nuclear and cytoplasmic markers was also used to evaluate fractionation quality.[35] One untreated nuclear sample (CTRL3) failed fractionation quality control and was excluded. Coverage tracks of nuclear and cytoplasmic reads were plotted with the trackViewer package.[89] We examined the motor neuron transcriptomic identities of iPSMNs using the ComplexHeatmap package based on the expression of canonical neuronal and glial cell type markers.

Differential transcript expression was fitted using the DESeq2 generalized linear model, utilizing the Wald test.[88] In all analyses, a transcript was considered significantly differentially expressed if the false discovery rate (FDR) < 0.05. Nuclear/cytoplasmic fold change was calculated using the design $\sim$ *sample* + *fraction* and result contrast formula $log\,2(Nuclear\ /\ Cytoplasmic)$. To compare differences in ALS versus control nuclear/cytoplasmic fold changes, while accounting for nuclear-cytoplasmic cell line pairing, we used a multi-factor design with interaction terms: $\sim fraction + genotype + genotype : cell\ line + fraction : genotype$. By including the terms "genotype" and "fraction" in the design, we can detect expression changes due to ALS versus control at the total (nuclear + cytoplasm) level (fraction-independent) as well as expression changes due to fraction (nuclear versus cytoplasm) across both ALS and control samples (genotype-independent). To identify changes in expression due to both fraction and genotype, we used the results formula contrast $log\,2(fraction.nuclear\ /\ genotype.ALS)$ The model finds the "interaction" in transcripts whose ALS versus control expression changes are significantly different between nuclear and cytoplasmic fractions. This two-factor comparison is more easily interpretable as $ALS\ nuclear\ /\ cytoplasm\ vs.\ control\ nuclear\ /\ cytoplasm$.

Nuclear redistributed transcripts were defined as FDR < 0.05 and log_2 fold change > 0 and cytoplasmic redistributed transcripts FDR < 0.05 and log_2 fold change < 0. This approach was used for both untreated and ML240-treated iPSMNs. Differences in transcript redistribution between the 4 mutant groups were compared using transcriptome-wide Pearson correlation of the Wald test statistic and were depicted in scatterplots. The overlap of differentially redistributed transcripts was tested statistically using the one-sided Fisher exact test and depicted in UpSet plots. Nuclear and cytoplasmic redistributed transcripts were used as input to functional enrichment analyses, which were used to identify enriched pathways using g:Profiler2 and depicted in bar charts with redundant terms manually removed. g:Profiler2 performs statistical enrichment analysis to find over-representation using the hypergeometric test with correction for multiple testing with all expressed genes used as background. g:Profiler2 searches Gene Ontology (GO; molecular functions, biological processes and cellular components), KEGG, REAC, WikiPathways, CORUM and Human phenotype ontology sources. In the functional enrichment bar charts, the top significant terms were manually curated by removing redundant terms. Transcript features including biotype, isoform length, and exon number were extracted from the GTF file. GC content and Phast conservation scores were acquired from the GenomicScores R package. Statistical analyses were performed using the Wilcoxon tests with Benjamini-Hochberg correction for multiple testing.

Differential expression results for postmortem spinal cord ALS were calculated by comparing ALS versus control samples, accounting in the design for the RNA library preparation method, gender and the site of the spinal cord tissue (cervical, thoracic or lumbar) with the formula $\sim$ *sequencing instrument* + *gender* + *sample source* + *condition*.

RNA-protein interactions

RNA-protein interactions were predicted using the expansive RNAct database (https://rnact.crg.eu/).[40] RNAct provides length-normalized interaction scores for almost 6 billion protein-RNA pairwise interactions, enabling full coverage of the RNA-binding proteome. To examine interaction scores from the RNA view, for each transcript we summed the interaction scores for all its protein interactions, thus normalizing for both the total number and confidence in each RNA-protein interaction. For the protein view, for each protein we calculated the sum of its interaction scores across all transcripts.

To validate RNAct findings, we examined CLIP data for crosslink events between RBPs and proteins. We utilized iCLIP data from 21 RBPs[90] and eCLIP data from HepG2, K562, and HeLa cells for 112 RBPs available from ENCODE.[91] The number of crosslink events between each RBP and each transcript were obtained using the GenomicRanges countOverlaps function and normalized for transcript length. To explore regional differences in transcript RBP binding, we performed countOverlaps on CLIP crosslink events with sequences of CDS, introns, 5′ UTR, and 3′ UTRs separately. RBP motif enrichment among redistributed transcripts was calculated using Transite (https://transite.mit.edu/), which performs a matrix-based Transcript Motif Set Analysis (TMSA) on 174 motifs from the RBPDB and CISBP-RNA databases.[41,42,92]

Alternative splicing

Alternative splicing was analyzed using MAJIQ v2.4.[43] STAR aligned BAMs were used as input to the MAJIQ splice graph builder using Ensembl GRCh38.99 GFF3 transcript annotation. Differential splicing was quantified using the *MAJIQ deltapsi* and *Voila tsv*. A threshold of 20% $\Delta\Psi$ and changing probability >90% was used to call significant splicing changes between ALS mutants and controls. Events were visualized using *Voila view*. Changes in each class of splicing were examined using *Voila modulize*, which breaks down local splice variants into binary splicing events (e.g. exon skipping or intron retention). For comparison of ALS iPSMN splicing events with ALS postmortem, NYGC samples were analyzed using the MAJIQ *heterogen* function, which is more appropriate for a large heterogeneous dataset with known batch effects.[93,94] Sequencing instrument, gender, and sample source batch effects were corrected for using *MOCCASIN*.[94] A threshold of 20% $\Delta\Psi$ and TNOM p value < 0.05 was used to call significant splicing changes between groups.

Proteome analysis

For analysis of mass spectrometry spectral intensities, LC-MS/MS raw files were processed in MaxQuant (version 2.0.3.1) and the peptide lists generated were searched against the reviewed UniProt human proteome using the Andromeda search engine embedded in MaxQuant.[95] Enzyme specificity for trypsin was selected (cleavage at the C-terminal side of lysine and arginine amino acid residues unless proline is present on the carboxyl side of the cleavage site) and a maximum of two missed cleavages were allowed. Cysteine carbamidomethylation was set as a fixed modification, while oxidation of methionine and acetylation of protein N termini were set as variable modifications. Peptides were identified with an initial precursor mass deviation of up to 10 ppm and a fragment mass deviation of 0.2 Da. For label-free protein quantitation (MaxLFQ), we required a minimum ratio count of 1, with two minimum and two average comparisons, which enabled the normalization of the dataset.[96] An FDR, determined by searching a reverse sequence database, of 0.01 was used at both the protein and peptide levels.

Data from the Maxquant analysis were analyzed for differential protein expression using the DEP package (v1.11.0), which is a wrapper around limma.[44] Protein identifications were filtered, removing hits to the reverse decoy database and proteins identified as modified peptides. We required that each protein be detected in at least two out of the three replicates. Protein LFQ intensities were normalized and missing values were imputed by values simulating noise around the detection limit using the default parameters. Differential protein enrichment analysis was performed using protein-wise linear models combined with a Bayesian regression-based approach that utilizes limma. A protein was considered significantly differentially expressed when FDR < 0.05. The same design formulae and results contrasts were used as with the transcriptome analysis. VCP co-immunoprecipitation mass spectrometry raw files were analyzed in the same way.

All boxplots show the median, hinges represent the 25th and 75th percentiles, and whiskers correspond to 1.5 times the interquartile range. Schematics were created with BioRender.com.